Department of Construction Sciences
Solid Mechanics

ISRN LUTFD2/TFHF-5253/2023-SE(1-PP)

Numerical Modelling of Combined Forming and Punching of Sheet Metal for Heat Exchanger Applications

Master's Dissertation by

Erik Stålbrand

Supervisors:
Håkan Hallberg, Division of Solid Mechanics
Mattias Månsson, Alfa Laval

Examiner:
Mathias Wallin, Division of Solid Mechanics

For information, address:
Division of Solid Mechanics, Lund University, Box 118, SE-221 00 Lund, Sweden
Webpage: www.solid.lth.se

Abstract

In this work a strategy for numerical simulation of punching during concurrent pressing of stainless steel sheet metal has been investigated accounting for the stress triaxiality and Lode angle parameter. Modelling of the damage evolution of a sheet metal is a useful tool within the field of engineering and materials science, and can provide useful information regarding material capabilities in a design process.

An inverse modelling approach was used, where both a material model and a damage model were developed. The damage model was developed using the GISSMO damage model (Generalized Incremental Stress State dependent damage MOdel) which incorporates the dependence on the stress triaxiality and the Lode angle parameter. The fracture strain is defined in the stress triaxiality and Lode angle parameter space as a surface and experiments were conducted to cover the space of the stress states. The modified Mohr-Coulomb fracture criterion was used to predict fracture strain in every stress state. The simulation software LS-DYNA was used for numerical modelling and the software LS-OPT was used to identify damage parameters.

The results show good agreement with experimental data but due to issues with stress state characterization of the experiments, further validation is necessary before the damage model can be used in practice. The results from this work show a strong potential for the inverse modelling approach to model the evolution of damage using GISSMO. It was concluded that, in order to accurately describe the material behavior during punching, experimental data from a wide variety of stress states is necessary and the results from this work highlight the need of complete and accurate experiments. These findings are important for future development of damage models.

Acknowledgement

First and foremost, I would like to express my deepest gratitude to my supervisors, Håkan Hallberg and Mattias Månsson, for their invaluable guidance, support, and patience throughout the course of this dissertation. I would like to extend my gratitude to Mikael Schill and Axel Hallén at DYNAmore Nordic and Mathias Agmell at Alfa Laval for their assistance and expertise throughout the completion of this thesis. Their feedback was instrumental in helping me complete this project. This work has not only given me knowledge and experience within a subject, but also an insight into practical engineering work and method development. Lastly, I would like to thank Alfa Laval for giving me the opportunity to work with an interesting and applicable subject.

Erik Stålbrand
Lund, Sweden
January 2023

Contents

1 Introduction

The present paper is concerned with modelling of the fracture behaviour of a punching process during forming of a sheet metal plate for a gasketed plate heat exchanger. In most engineering applications, such as sheet metal forming, there is no interest in studying the material behavior until complete fracture. Instead, forming limit diagrams (FLDs) are commonly used to estimate sheet metal formability. However, when damage to the material is required in order to achieve a purpose it is crucial to understand and predict the material behavior from initial deformation until fracture. FLDs do not describe the fracture behavior of a material, they only predict whether or not the material will fracture [1]. A damage model on the other hand, describes the material degradation until complete fracture. The problem at hand is approached using an inverse modelling technique where experimental data is used to define the material behavior.

1.1 Alfa Laval

Alfa Laval is a global provider of products within heat transfer, separation and fluid handling and acts in three areas, the energy sector, food & water industry and the marine industry. Alfa Laval was founded in 1883 in Dalarna, Sweden, by Gustaf de Laval. Initially, the company name was AB Separator which was changed to Alfa Laval AB in 1963. In 1938 Alfa Laval introduced its first heat exchanger and the development and production was moved to Lund where it remains to this day [2].

1.2 Aim and objective

The aim of this thesis is to propose and investigate a strategy for numerical simulation of punching during concurrent pressing of stainless steel sheet metal for heat exchanger applications. The objective is to accurately model and predict the fracture evolution behavior and develop a method for designers to use in the forming process of plates for heat exchangers.

1.3 Confidential information

Some information in this report has been altered or removed due to confidentiality. This includes experimental data and sensitive information regarding numerical values related to both the material model and the damage model.

1.4 Limitations

The thesis is limited to studying the punching process in a forming simulation. A limited set of material test data is used in the work where no rate dependency is taken into account and the work is restricted by the available methods and material models in the software

LS-DYNA. Furthermore, the previously obtained experimental test data is incomplete and limits the material modelling.

2 Theory

2.1 Layout and working principles of heat exchangers

The goal of this thesis work is to develop a numerical method that is applicable to heat exchanger development. The main purpose of a heat exchanger is to heat or cool one medium by transferring heat between it and another. A heat exchanger consists of a number of corrugated plates that are fitted and sealed with rubber gaskets. The gaskets direct the hot and cold fluids in an alternating manner between every other plate in order to achieve the most efficient thermal performance [3]. In figure 1 a plate heat exchanger is illustrated.

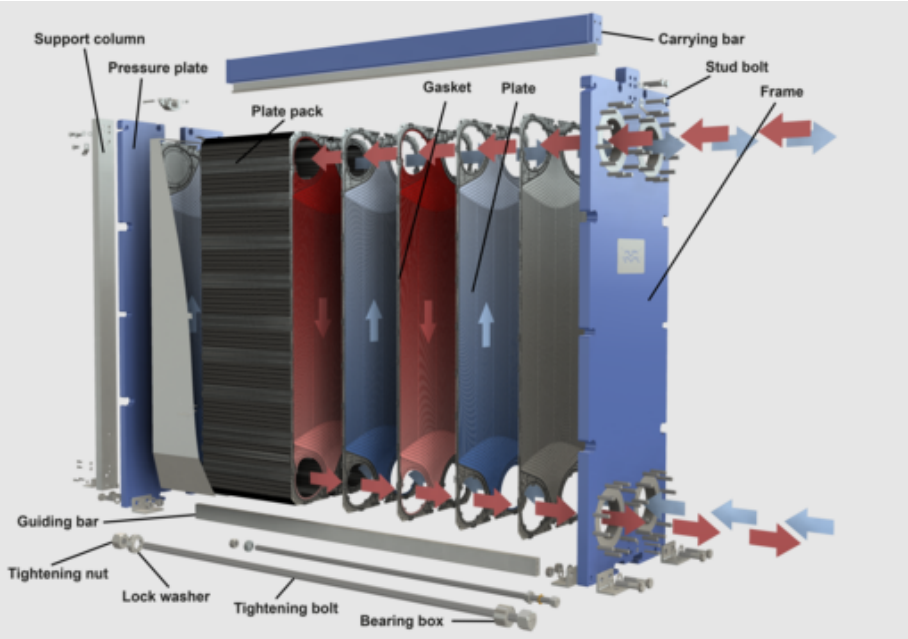

Figure 1: Plate heat exchanger [3].

2.2 Stress and strain

Stress and strain are used to describe the load and deformation at an arbitrary point on, or within, a body. In this section, the relationship between stress and strain is described as well as how the stress state of a body is defined.

When studying material behaviour by uniaxial tensile or compressive testing, the relationship between stress and strain can be presented as a stress-strain curve, which reveals a number of material characteristics, such as the modulus of elasticity, yield strength and ultimate strength. When performing this type of testing, a force is applied to a specimen and the displacement is measured as the load magnitude increases gradually. As the geometry of the specimen influences the displacement response of the material, it is of interest to convert the force- and displacement values into stress- and strain values, respectively. These

quantities are independent of specimen size and geometry. Uniaxial normal stress can be defined as the force per unit area according to

$$\sigma_{eng} = \frac{F}{A_0} \tag{1}$$

where F is the applied load and A_0 is the initial cross-sectional area of the specimen. The uniaxial normal strain can be defined as the change in length of the specimen divided by the initial length as

$$\varepsilon_{eng} = \frac{L - L_0}{L_0} = \frac{\delta}{L_0} \tag{2}$$

where L is the current length and L_0 is the initial length. The subscript eng refers to engineering stress and strain which is commonly used in engineering applications. However, as a uniaxial tension or compression test specimen is subject to a load, the cross-sectional area changes, meaning that the engineering stress-strain relationship is a simplification of reality. Instead, the true stress can be used which is defined as

$$\sigma = \frac{F}{A} \tag{3}$$

where A is the current cross-sectional area. The engineering strain can be related to the true strain, assuming a constant volume of the specimen, as

$$\varepsilon = \ln(1 + \varepsilon_{eng}) \tag{4}$$

The ultimate strength, also referred to as the point of necking or the point of instability, occurs at maximum engineering stress. At this point the strain will localize in a small region [4].

To describe the full 3D stress state of a body the stress tensor must be introduced. The stress tensor describes the stresses in an arbitrary point on a continuum body and can be divided into two parts, one hydrostatic part and one deviatoric part. The stress tensor is defined in terms of traction vectors containing the stress components acting on a surface section of a body. The traction vectors can, in directions perpendicular to the coordinate axes, be expressed as

$$\boldsymbol{t}_1^T = \begin{bmatrix} \sigma_{11} & \sigma_{12} & \sigma_{13} \end{bmatrix} \tag{5}$$

$$\boldsymbol{t}_2^T = \begin{bmatrix} \sigma_{21} & \sigma_{22} & \sigma_{23} \end{bmatrix} \tag{6}$$

$$\boldsymbol{t}_3^T = \begin{bmatrix} \sigma_{31} & \sigma_{32} & \sigma_{33} \end{bmatrix} \tag{7}$$

where σ_{11}, σ_{22} and σ_{33} are normal stresses and σ_{12}, σ_{13}, σ_{21}, σ_{23}, σ_{31} and σ_{32} are shear

stresses acting on a surface as shown in figure 2 [5].

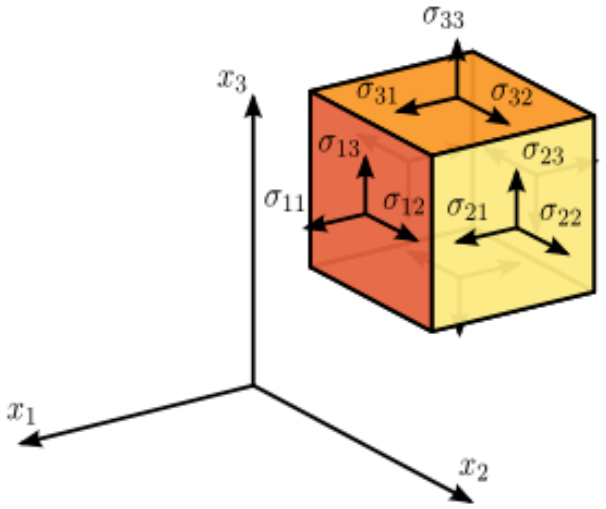

Figure 2: Stress components of the Cauchy stress tensor [6].

The traction vectors can be combined to form the Cauchy stress tensor

$$\left[\boldsymbol{\sigma}_{ij}\right] = \begin{bmatrix} \boldsymbol{t}_1^T \\ \boldsymbol{t}_2^T \\ \boldsymbol{t}_3^T \end{bmatrix} = \begin{bmatrix} \sigma_{11} & \sigma_{12} & \sigma_{13} \\ \sigma_{21} & \sigma_{22} & \sigma_{23} \\ \sigma_{31} & \sigma_{32} & \sigma_{33} \end{bmatrix} \tag{8}$$

The part of the stress tensor that acts to change the volume of the body is called the hydrostatic stress which is a scalar quantity and is defined as

$$\sigma_H = \frac{\sigma_{11} + \sigma_{22} + \sigma_{33}}{3} \tag{9}$$

where the numerator is the first Cauchy-stress invariant, I_1 [5]. The hydrostatic stress can be represented in the Haigh–Westergaard stress space by a position along the hydrostatic axis where $\sigma_{11} = \sigma_{22} = \sigma_{33}$ as illustrated in figure 3 below.

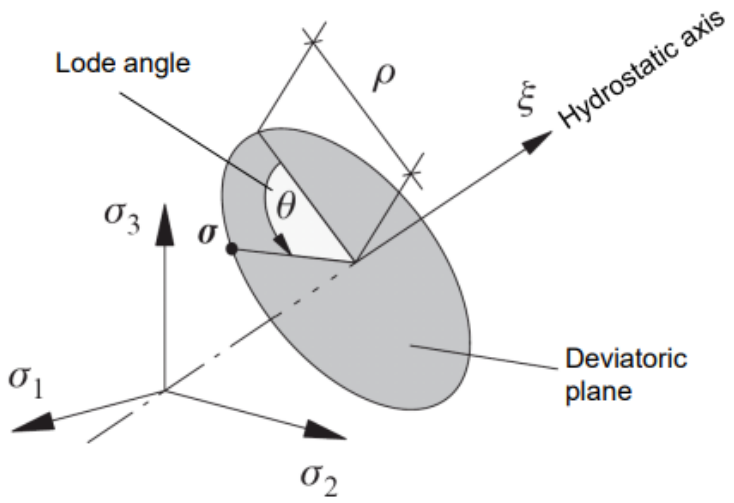

Figure 3: Haigh-Westergaard stress space [7].

From the eigenvalue problem of the hydrostatic part of the stress tensor the hydrostatic stress invariants I_1, I_2 and I_3 can be defined as

$$I_1 = \sigma_{ii}, \qquad I_2 = \frac{1}{2}\sigma_{ij}\sigma_{ji}, \qquad I_3 = \frac{1}{3}\sigma_{ij}\sigma_{jk}\sigma_{ki} \tag{10}$$

The hydrostatic stress invariants are used to describe the stress state in terms of triaxiality.

The part of the stress tensor responsible for the non-volumetric distortion of the body is the deviatoric stress which contains the shear stresses [5]. It can be defined by subtracting the hydrostatic stress from the stress tensor as

$$s_{ij} = \sigma_{ij} - \frac{1}{3}\sigma_{kk}\delta_{ij} = \begin{bmatrix} \sigma_{11} - \sigma_H & \sigma_{12} & \sigma_{13} \\ \sigma_{21} & \sigma_{22} - \sigma_H & \sigma_{23} \\ \sigma_{31} & \sigma_{32} & \sigma_{33} - \sigma_H \end{bmatrix} \tag{11}$$

The deviatoric stress can be represented in the Haigh–Westergaard stress space as the deviatoric plane, which is illustrated in figure 3.

The deviatoric stress invariants J_1, J_2 and J_3 can be defined as

$$J_1 = s_{ii} = 0, \qquad J_2 = \frac{1}{2}s_{ij}s_{ji}, \qquad J_3 = \frac{1}{3}s_{ij}s_{jk}s_{ki} \tag{12}$$

The deviatoric stress invariants can be obtained directly from the stress tensor and are used to define the Lode angle parameter which, together with the stress triaxiality, is used to define the stress state of a body.

The fracture strain of a material has been shown to be dependent on the stress state [8]. This dependency is described using the dimensionless stress triaxiality parameter. It is defined as

the ratio between the mean stress and the equivalent von Mises stress and can be expressed as

$$\eta = \frac{\sigma_m}{\sigma_{eq}} = \frac{\frac{1}{3}(\sigma_1 + \sigma_2 + \sigma_3)}{\sqrt{\frac{1}{2}\left(\sigma_1 - \sigma_2\right)^2 + (\sigma_2 - \sigma_3)^2 + (\sigma_3 - \sigma_1)^2}}$$

from which it can be identified that the mean stress is the previously described hydrostatic stress [9].

Studies conducted by [10] and [11] concluded that not only the hydrostatic stress has an impact on the fracture strain, but also the Lode angle parameter should be included in the constitutive material description. The Lode angle parameter can be described in terms of the normalized third deviatoric stress invariant ξ. The Lode angle is illustrated in the principal stress space in figure 3 as an angle in the deviatoric plane. The normalized third deviatoric stress invariant can be expressed as

$$\xi = \frac{27}{2}\frac{J_3}{\sigma_{eq}^3} \tag{14}$$

which is then related to the Lode angle as

$$\xi = \cos(3\theta) \tag{15}$$

The Lode angle can then be normalized and expressed as

$$\overline{\theta} = 1 - \frac{2}{\pi}\arccos(\xi) \tag{16}$$

Since the Lode angle θ varies between $0 \leq \theta \leq \frac{\pi}{3}$, the Lode angle parameter $\overline{\theta}$ varies between $-1 \leq \overline{\theta} \leq 1$ [11]. Together with the triaxiality, the Lode angle parameter defines a fracture envelope in the principal stress space [10].

2.3 Damage mechanics

Damage mechanics is a branch of mechanics concerning prediction of fracture initiation, crack propagation and fracture of materials. Experiments have shown that ductile fracture is generally a three-step process: (a) accumulation of damage; (b) fracture initiation; and (c) crack propagation. The fracture initiation occurs due to the accumulation of damage which can be considered microscopically and macroscopically. On a microscopical scale damage is observed as nucleation, growth and coalescence of voids. On a macroscopical scale however, damage can be observed as the loss of load-bearing capacity of a material in terms of decreased stiffness, strength and reduced ductility [10].

This work is focused on the macroscopical scale of damage and uses a continuum damage mechanics approach, meaning that the material is idealized as a continua. The accumulation of damage is described by an internal damage variable which is a scalar quantity and will be further presented in section 2.7 along with damage modelling approaches.

2.3.1 Ductile fracture

There are two fundamental types of fracture in metals, brittle fracture and ductile fracture, where the latter will be discussed here due to its relevance to this work. Material failure in ductile solids is mainly caused by nucleation, growth and coalescence of voids as a result of an applied load. The nucleation of voids can be seen on a microscopic level and is the result of either decohesion at the boundary between a particle and the matrix, or by particle cracking during material deformation. After void nucleation, the voids grow as a result of an applied load that changes their size and shape. The voids will continue to grow until a critical distance between them is reached and the matrix between them fails which results in microcracks. The cracks then propagate due to void coalescence [12].

Due to its industrial importance, the field of ductile fracture has been of interest for many researchers over the last 70 years [13]. The focus of the research has been on how the stress state of a metal controls the ductile fracture. Among others, [8] concluded that ductile fracture, measured as equivalent strain to fracture, is strongly dependent on stress triaxiality. However, through experimental observations it has been concluded that the proposed fracture models that take only triaxiality into account cannot describe the fracture behaviour over a large range of triaxialities. This has led to the introduction of the Lode angle parameter into the fracture models [14].

In sheet metal forming, forming limit diagrams are used to evaluate necking and thinning of sheet metal plates. A forming limit diagram describes whether or not the material will fracture which is insufficient when the fracture development and crack propagation is of interest [1]. Damage models on the other hand, describe the material degradation on a more detailed level and, for the applications in this work where the fracture is implied, the FLD loses its relevance.

2.4 Materials testing

Physical experiments have been conducted to lay the foundation for the damage model in this work. In the experiments, the specimens have a thickness of 0.5 mm and are designed such that they each represent a different stress state, as described by the Lode angle parameter and the stress triaxiality. From each experiment a fracture strain can be found, which will then lay the foundation of the three-dimensional fracture locus. The tests are conducted in a quasi-static manner and are performed to provide a plane stress state. Each test is performed in the rolling direction of the material, which provides insufficient data to completely define

the material model in terms of material anisotropy. Previous material tests are used to make up for the missing data. All geometries that were used in the experiments will be presented and described in this section.

2.4.1 Uniaxial tensile test

In the uniaxial tensile test, a flat specimen shaped like the one in figure 4 is loaded into a tensile test machine where both ends are clamped. A uniaxial load is applied to both ends and the elongation of the specimen and the applied force are measured. The shape of the specimen confines the deformation to the center where the fracture eventually occurs. From the information obtained in the tensile test the stresses, strains, Poisson's ratio and stiffness of the material can be obtained [15]. The uniaxial tensile test is designed to, in theory, describe the stress state at triaxiality $\eta = \frac{1}{3}$ and Lode angle parameter $\overline{\theta} = 1$.

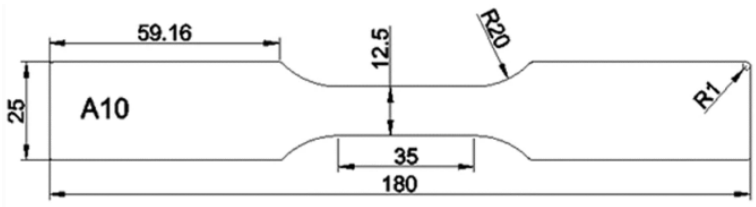

Figure 4: Geometry of uniaxial tensile test used for experiment [16].

2.4.2 Plane strain

The plane strain test has a notch which localizes the stress and restricts the lateral contraction and therefore the formation of a neck, as opposed to the uniaxial tensile test, will not take shape. The plane strain test is performed the same way as the uniaxial tensile test. It is designed to be in a stress state of triaxiality $\eta = \frac{1}{\sqrt{3}}$ and Lode angle parameter $\overline{\theta} = 0$ and is illustrated in figure 5.

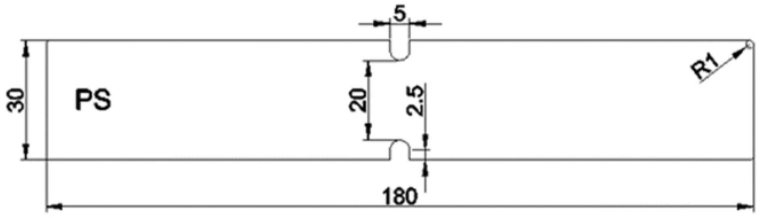

Figure 5: Geometry of plane strain test used for experiment [16].

2.4.3 Shear test

The geometry of the shear test is designed such that the specimen experiences a shear failure parallell to the load direction. The shear test is performed in the same manner as the

uniaxial tensile and plane strain tests. It should in theory be in a stress state of triaxiality $\eta = 0.1$ and have Lode angle parameter $\overline{\theta} = 0$ and is illustrated in figure 6.

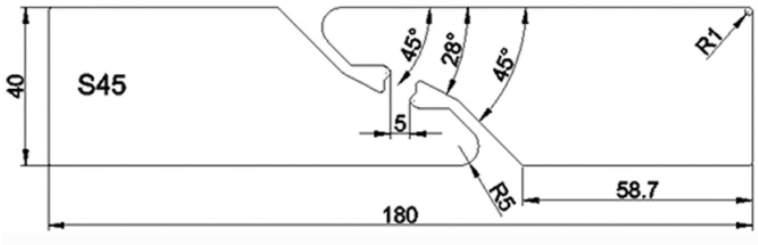

Figure 6: Geometry of general shear test used for experiment [16].

2.4.4 Biaxial bulge test

The biaxial bulge test is a Nakajima test designed to describe a stress state of triaxility $\eta = 0.67$ and a Lode angle parameter $\overline{\theta} = -1$. It consists of a circular metal sheet clamped between a die and a holder that is stretched using a hemispherical punch as presented in figure 7.

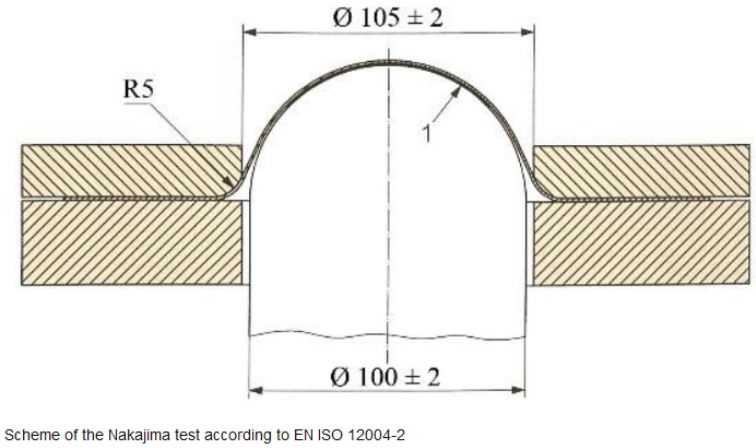

Figure 7: Geometry of biaxial tension test used for experiment [16].

2.4.5 Digital Image Correlation

From the experiments described above, data is extracted using Digital Image Correlation (DIC), which is a non-contact optical technique for measuring displacement. In a subsequent step, strain fields can be evaluated from the measured displacements. The method makes use of digital cameras that register the course of deformation of a test specimen. On the specimen surface a speckle pattern is applied, for example using spray paint, which the software uses to map the shape and deformation of the object using the commercial software ARAMIS. From the deformation field, the strain field is determined which is then used to determine the strain tensor at every point [17].

2.4.6 Anisotropy

The data provided by the material tests is not enough to define the material model as the tensile tests have been performed only in the rolling direction. However, in previous material testing used to calibrate a material model the 316 steel has shown anisotropic characteristics, meaning that is has directionally dependent properties. This is therefore taken into account in this work as well. The anisotropy is described by the yield stresses in different directions and the Lankford coefficients. The yield stress in the rolling direction is obtained from experimental data using a condition such as the 0.2% offset yield strength. The yield stresses in other directions than the rolling direction are obtained using a scale factor determined by the quotient between the yield stress in the rolling direction from the new experiments and the yield stress from the old experiments. The Lankford coefficient, or the R-value, is defined as the ratio between width strain and thickness strain as

$$R = \frac{\varepsilon_w}{\varepsilon_t} \tag{17}$$

where the rolling direction is perpendicular to both the width and thickness. The forming ability for rolled sheet metals is defined by the normal anisotropy ratio, which is determined using three directions relative to the rolling direction as

$$R_m = \frac{R_0 + 2R_{45} + R_{90}}{4} \tag{18}$$

where R_0, R_{45} and R_{90} are the Lankford coefficients in different directions relative to the rolling direction [18].

2.4.7 The Least-squares criterion

This work is approached using an inverse modelling technique, meaning that experimental data is used to obtain parameter values that define the system, i.e. the damage parameters. To solve the inverse modelling problem, the least-squares method is used which minimizes an objective function which is the residual sum of the squares, hence the name of the method. The residuals are defined as the difference between a given data set of n values, $y_1, ..., y_n$ and a fitted model f consisting of values $f_1, ..., f_n$ as

$$e_i = y_i - f_i \tag{19}$$

and the mean of the data is defined as

$$\overline{y} = \frac{1}{n}\sum_{i=1}^{n} y_i \tag{20}$$

The correlation between the data and the fitted model can then be measured with two sums

of squares, namely the residual sum of squares SS_{res} and the total sum of squares SS_{tot}, defined as

$$SS_{res} = \sum_i (y_i - f_i)^2 = \sum_i e_i^2 \tag{21}$$

and

$$SS_{tot} = \sum_i (y_i - \overline{y})^2 \tag{22}$$

By combining these values the coefficient of determination R^2 can be defined from which the correlation between the given data set and the fitted line can be obtained. The coefficient is defined as

$$R^2 = 1 - \frac{SS_{res}}{SS_{tot}} \tag{23}$$

and is a measure of how well the dependent variable correlates to the independent variable [19].

2.5 The finite element method

To study the fracture behavior of the plate, differential equations are used to describe the physical problem mathematically. The solution to the system of differential equations cannot be obtained analytically and is instead found numerically, by dividing the domain into smaller parts, finite elements, which are used to approximate the solution of the boundary value problem in each element. In order to solve arbitrary differential equations they first have to be reformulated into an equivalent form, the so-called weak formulation and thereafter into the FE-formulation, which is presented in this section. Further details can be found in [5].

2.5.1 Strong formulation

After introducing the connection between the traction vector and the stress tensor in section 2.2, the equations of motion for an arbitrary point on a surface S of a body with volume V can be formulated. The outer forces acting on the surface are summarized in the traction vector t_i and the body forces per unit volume are summarized in the vector b_i. The displacement is denoted u_i and the acceleration becomes $\ddot{u}_i$, with two superposed dots denoting the second derivative with respect to time. Newton's second law of motion states that

$$\int_S t_i dS + \int_V b_i dV = \int_V \rho \ddot{u}_i dV \tag{24}$$

where ρ is the density. In order to reformulate this equation for an arbitrary region we use the divergence theorem of Gauss which, for an arbitrary vector $\boldsymbol{q}$, states that

$$\int_V q_{i,i} dV = \int_S q_i n_i dS \tag{25}$$

This relation can be generalized to an arbitrary quantity c_{ij} as

$$\int_V c_{ij,j} dV = \int_S c_{ij} n_j dS \tag{26}$$

Using equation (26), we can reformulate equation (24) to obtain

$$\int_V (\sigma_{ij,j} + b_i - \rho \ddot{u}_i) dV = 0 \tag{27}$$

which holds for arbitrary regions of a body, and can be simplified as

$$\sigma_{ij,j} + b_i = \rho \ddot{u}_i \tag{28}$$

which expresses the equations of motion and is the strong finite element formulation.

2.5.2 Weak formulation

From the equations of motion, i.e. the strong formulation in equation (28), we can derive the weak formulation by multiplying equation (28) by an arbitrary weight vector v_i and integrate over the volume V to obtain

$$\int_V v_i (\sigma_{ij,j} + b_i - \rho \ddot{u}_i) dV = 0 \tag{29}$$

which we rewrite into

$$\int_V \left[(\sigma_{ij} v_i)_{,j} - \sigma_{ij} v_{i,j} \right] dV + \int_V (v_i b_i - \rho v_i \ddot{u}_i) dV = 0 \tag{30}$$

If we utilize the divergence theorem of Gauss from equation (25) and obtain

$$\int_V (\sigma_{ij} v_i)_{,j} dV = \int_S \sigma_{ij} v_i n_j dS = \int_S v_i t_i dS \tag{31}$$

By using equation (31) in equation (30), we obtain

$$\int_V \rho v_i \ddot{u}_i dV + \int_V v_{i,j} \sigma_{ij} dV = \int_S v_i t_i dS + \int_V v_i b_i dV \tag{32}$$

Since the vector v_i is arbitrary and unrelated to the displacement vector u_i, we use the quantity

$$\varepsilon^v_{ij} = \frac{1}{2}(v_{i,j} + v_{j,i}) \tag{33}$$

which is the strain associated with the vector v_i in the same manner as the strain tensor ε_{ij} is related to the displacement vector u_i. By using the symmetry properties of σ_{ij} we obtain

$$v_{i,j}\sigma_{ij} = \frac{1}{2}(v_{i,j}\sigma_{ij} + v_{j,i}\sigma_{ji}) = \frac{1}{2}(v_{i,j}\sigma_{ij} + v_{j,i}\sigma_{ij}) = \varepsilon^v_{ij}\sigma_{ij} \tag{34}$$

which we use to rewrite equation (32) to obtain the weak formulation of the equations of motion as

$$\int_V \rho v_i \ddot{u}_i dV + \int_V \varepsilon^v_{ij}\sigma_{ij} dV = \int_S v_i t_i dS + \int_V v_i b_i dV \tag{35}$$

2.5.3 FE-formulation

By rewriting the weak formulation presented in equation (35) on matrix form we obtain

$$\int_V \rho \boldsymbol{v}^T \ddot{\boldsymbol{u}} dV + \int_V (\boldsymbol{\varepsilon}^v)^T \boldsymbol{\sigma} dV = \int_S \boldsymbol{v}^T \boldsymbol{t} dS + \int_V \boldsymbol{v}^T \boldsymbol{b} dV \tag{36}$$

where the displacement vector $\boldsymbol{u}$ can be expressed as

$$\boldsymbol{u} = \boldsymbol{N}\boldsymbol{a} \tag{37}$$

where $\boldsymbol{N}$ contains the global shape functions and $\boldsymbol{a}$ includes all nodal displacements of the body. From the time dependence of the displacements it follows that

$$\ddot{\boldsymbol{u}} = \boldsymbol{N}\ddot{\boldsymbol{a}} \tag{38}$$

From the displacements given by equation (37) the strains can be expressed using the matrix $\boldsymbol{B}$, which is derived from the matrix $\boldsymbol{N}$, as

$$\boldsymbol{\varepsilon} = \boldsymbol{B}\boldsymbol{a} \tag{39}$$

The arbitrary weight vector $\boldsymbol{v}$ is chosen using the Galerkin method, meaning that it is approximated in the same manner as the displacements $\boldsymbol{u}$. Due to this we can express the weight function as

$$\boldsymbol{v} = \boldsymbol{N}\boldsymbol{c} \tag{40}$$

where vector $\boldsymbol{c}$ is arbitrary, just like $\boldsymbol{v}$. From this relation we can determine the strains as

$$\boldsymbol{\varepsilon}^{\boldsymbol{v}} = \boldsymbol{B}\boldsymbol{c} \tag{41}$$

With the use of equation (40) and equation (41) in the weak form equation (35) while noting that $\boldsymbol{c}$ is independent of position, we obtain

$$\boldsymbol{c}^{\boldsymbol{T}}\left[\int_V(\rho\boldsymbol{N}^{\boldsymbol{T}}\boldsymbol{N}dV)\ddot{\boldsymbol{a}}+\int_V\boldsymbol{B}^{\boldsymbol{T}}\boldsymbol{\sigma}dV-\int_S\boldsymbol{N}^{\boldsymbol{T}}\boldsymbol{t}dS-\int_V\boldsymbol{N}^{\boldsymbol{T}}\boldsymbol{b}dV\right]=0 \tag{42}$$

Since this relation holds for arbitrary $\boldsymbol{c}$-matrices, it can be concluded that

$$\boldsymbol{M}\ddot{\boldsymbol{a}}+\int_V\boldsymbol{B}^{\boldsymbol{T}}\boldsymbol{\sigma}dV=\boldsymbol{f} \tag{43}$$

where $\boldsymbol{M}$ can be defined as

$$\boldsymbol{M}=\int_V\rho\boldsymbol{N}^{\boldsymbol{T}}\boldsymbol{N}dV \tag{44}$$

and $\boldsymbol{f}$ defines the external forces according to

$$\boldsymbol{f}=\int_S\boldsymbol{N}^{\boldsymbol{T}}\boldsymbol{t}dS+\int_V\boldsymbol{N}^{\boldsymbol{T}}\boldsymbol{b}dV \tag{45}$$

The expression in equation (43) holds for any constitutive relation and is the FE-approximation that is the foundation of the numerical analyses in this work.

2.5.4 Contact modelling

The purpose of this work is to develop a method to predict material behaviour in a cutting or punching process. Due to this, a relevant part of the numerical modelling is contact modelling. There are several ways to model contact and here only the penalty method will be presented as it is exclusively used in this thesis work. In a penalty contact formulation the two bodies in contact are allowed to penetrate each other and depending on the penetration depth there will be a corresponding contact force, which acts like a spring in tension. In figure 8 the penalty contact method is illustrated where the slave surface penetrates the master surface.

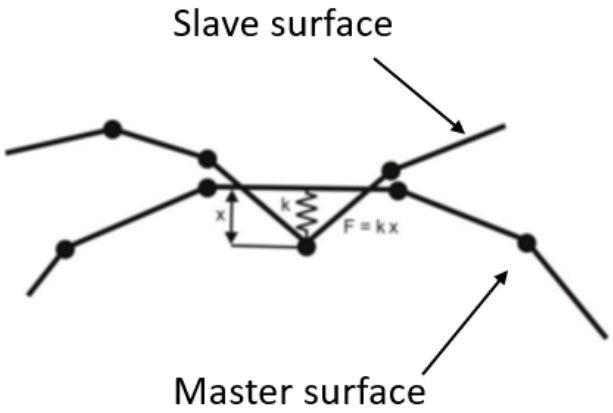

Figure 8: Penalty contact illustrating the slave surface penetrating the master surface. F - contact force, k - contact stiffness, x - penetration distance [20].

As can be seen in figure 8, the contact force is proportional to the penetration depth. A one-way contact is used due to its appropriateness when the master side of the contact is a rigid body, such as a a punch or die in a stamping simulation. In one-way contacts only the slave nodes are checked for penetration through the master surface and a Coulomb friction formulation is used to define the tangential contact behavior [21].

2.5.5 Friction modelling

When contact conditions are present in finite element modelling an important aspect is friction modelling. There is a number of approaches to account for friction effects and the simplest and most commonly used is the Coulomb friction formulation. Coulomb friction is a friction model defined by a constant force opposite to the direction of motion and independent of the velocity and can be expressed as

$$F_f = \mu F_N \tag{46}$$

where μ is the Coulomb friction coefficient and F_n is the normal force. The Coulomb friction model does not take dynamic effects into account and it simplifies the phenomenon of friction as it assumes that the frictional force is proportional to the normal force, independently of the contact area. It is limited in that it cannot take a unique value of friction at zero velocity. It is a simplified and efficient method of calculating the frictional force and is, despite its flaws, commonly used in engineering problems [22]. In figure 9 the Coulomb friction force is illustrated as a function of velocity.

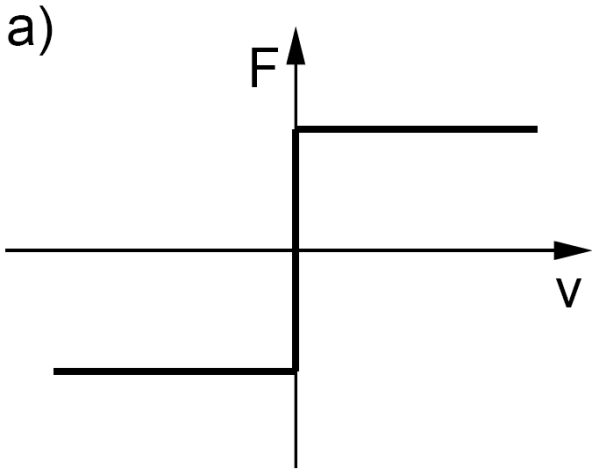

Figure 9: The friction force described by the Coulomb formulation [22].

2.5.6 Mass scaling

Finite element simulation times are dependent on the size of the model and the time step. In general, the model size is static so in order to reduce the simulation run time the time step has to be increased. An efficient method of doing this is to use mass scaling, which is a way to add nonphysical mass to a model in order to reduce the run time of the simulation. For an explicit integration scheme to be stable, there is a critical time step that must be maintained. The critical time step can be defined as

$$\Delta t_{min} = L_{min} / \sqrt{\frac{E(1-\nu)}{\rho(1+\nu)(1-2\nu)}} \tag{47}$$

where L_{min} is the minimum length of an element, ρ is the material density, E is the Young's modulus and ν is Poisson's ratio. From the critical time step we can obtain the minimum number of incremental steps in the solution according to

$$n_{min} = \frac{T}{\Delta t_{min}} \tag{48}$$

where T is the total forming time. From equation (48) it can be seen that, in order to reduce the number of incremental steps, it is necessary to either reduce the forming time or increase the critical time step. Since the forming time is generally fixed, the remaining option is to increase the critical time step. Without modifying the element size, this can be done by adding non-physical mass to increase density. In equation (47) it can be seen that by increasing material density, an increase in time step follows [23]. Excessive mass scaling may introduce dynamic problems such as oscillations in the solution and may stop the calculation from converging. In LS-DYNA the mass scaling is applied to those elements whose time step would otherwise be less than the specified value and not every element in

the model.

2.6 Constitutive modelling

A constitutive model contains the mathematical description of how a material responds to loads and uses stress-strain relations to formulate the governing equations. Constitutive modelling is an intensely researched field within solid mechanics and a few concepts relevant to this work are presented in this section.

2.6.1 Plasticity

Plasticity theory is a non-linear, time independent material behavior where strains remain in the material after unloading. These residual strains are referred to as plastic strains. Strain can be divided into two parts, namely elastic strain and plastic strain, which together make the total strain as

$$\varepsilon = \varepsilon^e + \varepsilon^p \tag{49}$$

where ε^e and ε^p represent the elastic strain and the plastic strain, respectively. In equation (49), the contribution from thermal strains has been neglected. The strain acts in a linear manner, proportional to the stiffness E until the yield stress is reached, after which plastic strain is developed. Using the linear relationship between stress and strain in the elastic region, the plastic strain can be defined as

$$\varepsilon^p = \varepsilon - \frac{\sigma}{E} \tag{50}$$

The plastic behavior is controlled by the material model which contains three important elements, namely the yield function, the hardening rule and the flow rule [5].

2.6.2 Yield criteria

The yield criterion for a material can be illustrated as a surface in the principal stress space. It defines the limit of elasticity and onset of plastic deformation for a material when subject to a load. If the stress state lies inside the surface the response is elastic and when the stress state lies on the surface it has reached the point of yielding, from which plastic deformation takes place [5]. There is a number of established yield criteria, such as the commonly used von Mises and Tresca formulations. In figure 10 the yield surfaces for the Tresca and von Mises yield criterion are illustrated. The yield criterion used in the present work is presented in connection to the material model in section 2.6.4.

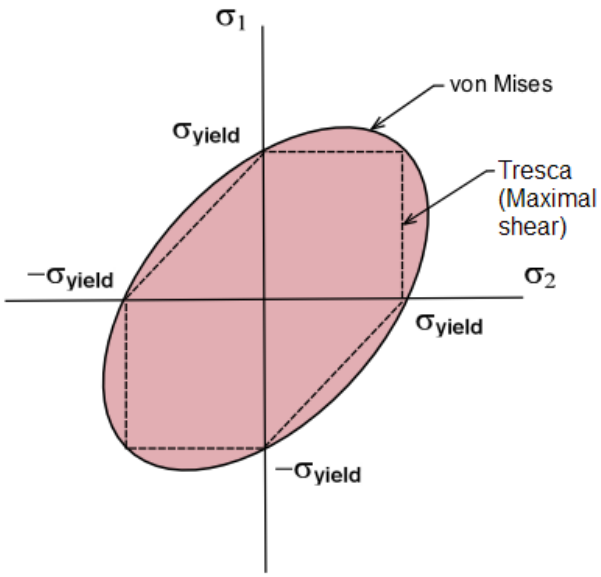

Figure 10: Tresca and von Mises yield surface in a two-dimensional stress space [24].

2.6.3 Hardening rule

The hardening rule describes how the yield surface changes with plastic loading. It can change isotropically, kinematically or by a mix between the two. For isotropic hardening, the yield surface remains in the same position and with the same shape but varies in size with plastic deformation. For kinematic hardening however, the yield surface has a fixed shape and size but its position changes with plastic deformation. In real load cases, it is common with a mixed hardening where the shape of the yield surface remains fixed while its size and position change with plastic deformation.

The yield surface shown in figure 10 can be described in terms of the hardening parameters K_α that determine how the yield surface changes with plastic deformation. The subscript α may refer to a number of hardening parameters that are either scalars or higher-order tensors. With this information we can express the yield surface as

$$f(\sigma_{ij}, K_\alpha) = 0 \tag{51}$$

where $K_\alpha = 0$ before plasticity is initiated. The third element that controls the plastic behaviour is the flow rule, which describes how the plastic strain evolves in a material and can be expressed as the constitutive relation

$$\dot{\varepsilon}^p_{ij} = \dot{\lambda}\frac{\partial f}{\partial \sigma_{ij}}; \qquad \dot{\lambda} \geq 0 \tag{52}$$

where $f = 0$ represents the yield surface, meaning that the plastic strain rate evolves in the normal direction to the yield surface in an incremental manner. The magnitude of the

plastic strain is determined by the plastic multiplier $\dot{\lambda}$ [5].

2.6.4 Barlat YLD2000

The material model used in this work is developed by [25] and has proven to be efficient and provide accurate results in sheet metal forming processes. It is a frequently used material model for forming simulations at Alfa Laval due to its flexibility regarding input parameters and applicability on different models using different element types. The yield surface for the material model is expressed as

$$f(\sigma, \alpha, \varepsilon_p) = \sigma_{eff}(\sigma_{xx} - 2\alpha_{xx} - \alpha_{yy}, \sigma_{yy} - 2\alpha_{yy} - \alpha_{xx}, \sigma_{xy} - \alpha_{xy}) - \sigma_Y^t(\varepsilon_p, \dot{\varepsilon}_p, \beta) \leq 0 \quad (53)$$

where the effective stress, σ_{eff} is defined as

$$\sigma_{eff}(s_{xx}, s_{yy}, s_{xy}) = \left[\frac{1}{2}(\varphi' + \varphi'')\right]^{(1/a)} \quad (54)$$

and the functions $\varphi^{'}$ and $\varphi^{''}$ are defined as

$$\begin{aligned} \varphi^{'} &= |X_1^{'} - X_2^{'}|^a \\ \varphi^{''} &= |2X_1^{''} + X_2^{''}|^a + |X_1^{''} + 2X_2^{''}|^a \end{aligned} \quad (55)$$

The exponent a is associated with the crystal structure of the material and $X_i^{'}$ and $X_i^{''}$ are eigenvalues of the linearly transformed deviatoric stresses $X_{ij}^{'}$ and $X_{ij}^{''}$, given by

$$\begin{aligned} X_1^{'} &= \frac{1}{2}\left(X_{11}^{'} + X_{22}^{'} + \sqrt{(X_{11}^{'} - X_{22}^{'})^2 + 4{X_{12}^{'}}^2}\right) \\ X_2^{'} &= \frac{1}{2}\left(X_{11}^{'} + X_{22}^{'} - \sqrt{(X_{11}^{'} - X_{22}^{'})^2 + 4{X_{12}^{'}}^2}\right) \end{aligned} \quad (56)$$

and

$$\begin{aligned} X_1^{''} &= \frac{1}{2}\left(X_{11}^{''} + X_{22}^{''} + \sqrt{(X_{11}^{''} - X_{22}^{''})^2 + 4{X_{12}^{''}}^2}\right) \\ X_2^{''} &= \frac{1}{2}\left(X_{11}^{''} + X_{22}^{''} - \sqrt{(X_{11}^{''} - X_{22}^{''})^2 + 4{X_{12}^{''}}^2}\right) \end{aligned} \quad (57)$$

The linear transformation of the deviatoric stresses is given by

$$
\begin{pmatrix} X'_{11} \\ X'_{22} \\ X'_{33} \end{pmatrix} = \begin{pmatrix} L'_{11} & L'_{12} & 0 \\ L'_{21} & L'_{22} & 0 \\ 0 & 0 & L'_{33} \end{pmatrix} \begin{pmatrix} s_{xx} \\ s_{yy} \\ s_{zz} \end{pmatrix}
$$
$$
\begin{pmatrix} X''_{11} \\ X''_{22} \\ X''_{33} \end{pmatrix} = \begin{pmatrix} L''_{11} & L''_{12} & 0 \\ L''_{21} & L''_{22} & 0 \\ 0 & 0 & L''_{33} \end{pmatrix} \begin{pmatrix} s_{xx} \\ s_{yy} \\ s_{zz} \end{pmatrix} \tag{58}
$$

where

$$
\begin{pmatrix} L'_{11} \\ L'_{12} \\ L'_{21} \\ L'_{22} \\ L'_{33} \end{pmatrix} = \frac{1}{3} \begin{pmatrix} 2 & 0 & 0 \\ -1 & 0 & 0 \\ 0 & -1 & 0 \\ 0 & 2 & 0 \\ 0 & 0 & 3 \end{pmatrix} \begin{pmatrix} \alpha_1 \\ \alpha_2 \\ \alpha_7 \end{pmatrix}
$$
$$
\begin{pmatrix} L''_{11} \\ L''_{12} \\ L''_{21} \\ L''_{22} \\ L''_{33} \end{pmatrix} = \frac{1}{9} \begin{pmatrix} -2 & 2 & 8 & -2 & 0 \\ 1 & -4 & -4 & 4 & 0 \\ 4 & -4 & -4 & 1 & 0 \\ -2 & 8 & 2 & -2 & 0 \\ 0 & 0 & 0 & 0 & 9 \end{pmatrix} \begin{pmatrix} \alpha_3 \\ \alpha_4 \\ \alpha_5 \\ \alpha_6 \\ \alpha_8 \end{pmatrix} \tag{59}
$$

The parameters α_1 to α_8 determine the shape of the yield surface and are calculated using a Newton-Raphson procedure [26]. In figure 11 the yield surface for the Barlat YLD2000 yield criteria is illustrated and compared to the von Mises yield criteria.

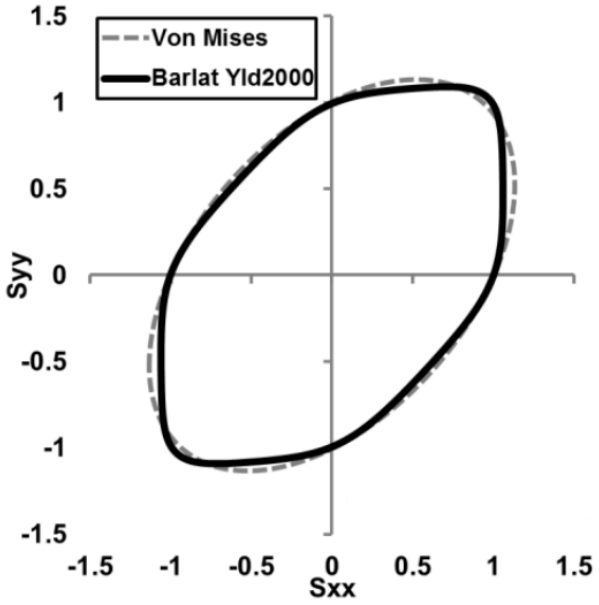

Figure 11: Illustration of a yield surface using the Barlat YLD2000 yield criteria compared with the von Mises yield criteria [27].

2.7 Damage modelling

Damage modelling is relevant when the material behavior beyond the point of instability is of interest. From initial loading until the point of instability the material behavior is described by the material model whereafter the damage model is coupled to the stress which controls the material degradation until the point of fracture. Beyond the instability point the solution is no longer unique and is mesh dependent. The concept of the damage modelling in this work is illustrated in figure 12.

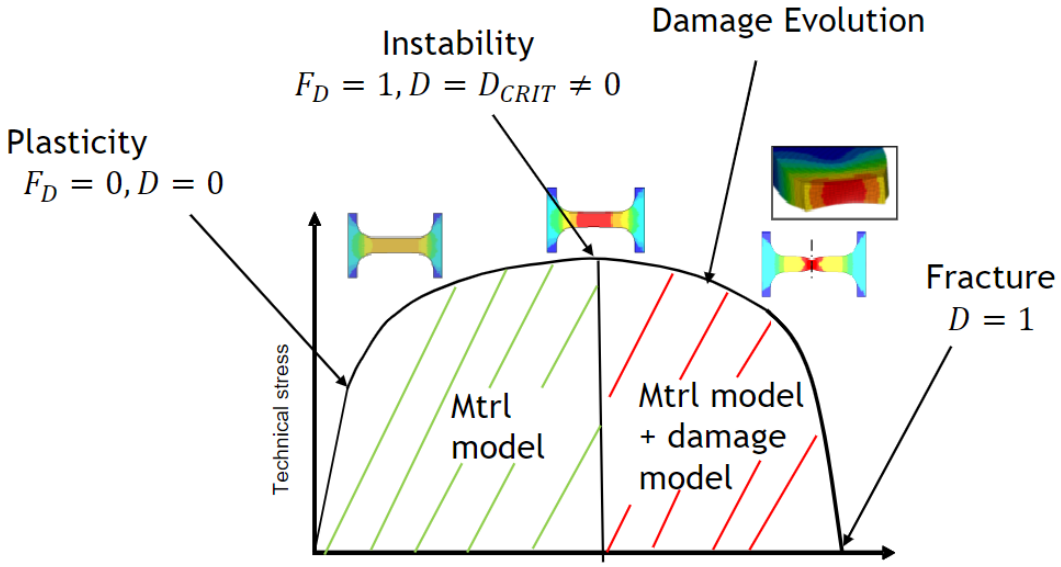

Figure 12: Connection between material model and damage model [28].

The instability parameter, F_D, and the damage variable, D, shown in figure 12, begin to evolve at the onset of plastic deformation. At the point of instability, the instability parameter reaches a value of one and the damage parameter reaches a critical value different from zero. At this point the damage is coupled to the stress and the material degradation is initiated. These parameters are further discussed in section 2.7.4. Damage evolution does not progress spontaneously after it has been initiated but requires a damage evolution model. Damage models can be divided into two branches, the physics-based models and the continuum mechanics models. A physics-based model is a physically sound model which incorporates physical mechanisms such as void growth and coalescence, such as the Gurson model, found in [29]. The continuum mechanics damage models are phenomenological and are controlled by certain conditions that are expressed in terms of parameters such as stress, strain or energy. It can be considered an engineering approach to damage mechanics as opposed to a more scientific model [30]. To model the damage initiation and propagation in this work, the damage model GISSMO (**G**eneralized **I**ncremental **S**tress **S**tate dependent damage **MO**del) is used which is a phenomenological model, meaning that it is consistent with fundamental theory, but not directly derived from it. The damage model was proposed

in [31] and is implemented in LS-DYNA and can be applied to any material model in the software.

2.7.1 Modelling of fracture

As mentioned previously, ductile fracture is dependent on the triaxiality and the Lode angle parameter. However, before the Lode angle parameter was introduced, only triaxiality was used to predict failure strain which, under plane stress assumption, is valid and is illustrated in figure 13.

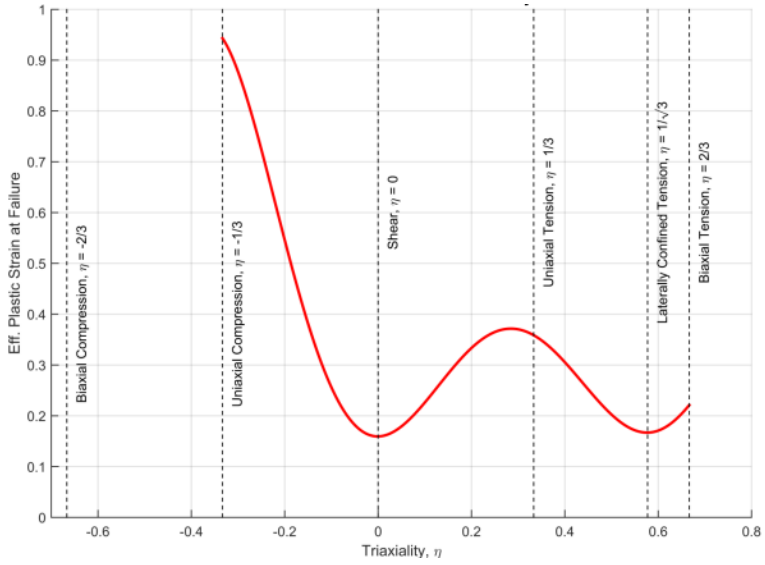

Figure 13: Hypothetical fracture strain in plane stress [32].

The response in figure 13 shows a typical behaviour of a plane stress case. For plane stress, where $\sigma_3 = 0$, it was shown in [33] that the stress triaxiality can be uniquely related to the Lode angle parameter by

$$\xi = cos\left[\frac{\pi}{2}(1-\bar{\theta})\right] = -\frac{27}{2}\eta(\eta^2 - \frac{1}{3}) \tag{60}$$

which means that only one of the parameters needs to be determined to describe the stress state, such as in figure 13. When the damage model is to be used in three dimensions, such as in a punching process, it is no longer a plane stress case and the triaxiality and Lode angle parameter become independent of each other. The result of adding the Lode angle parameter is that instead of a failure curve as presented in figure 13, a surface is required to define the failure, as illustrated in figure 14.

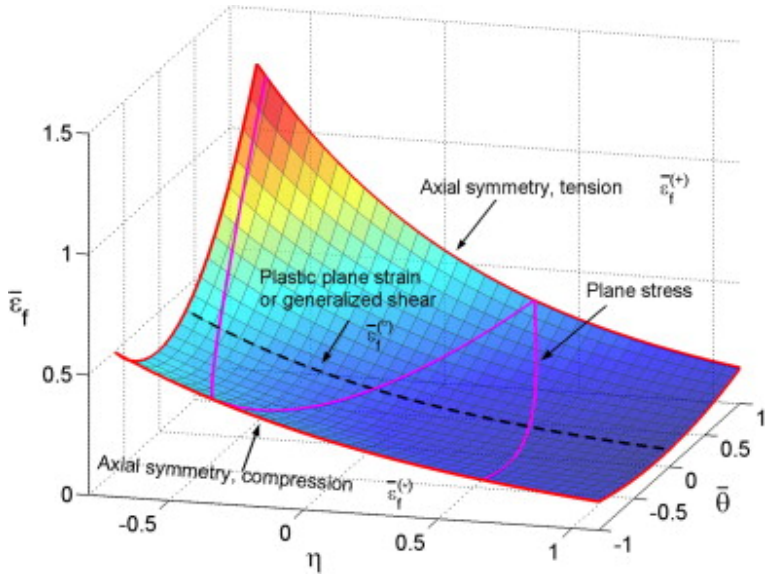

Figure 14: Three-dimensional fracture surface dependent on triaxiality and the Lode angle parameter [11].

As can be seen in figure 14, the plane stress and plane strain stress states are included which shows the limitation of using shell elements and a plane stress assumption.

2.7.2 Damage evolution

Material damage can be described as the loss of load bearing capacity of a material and from a continuum point of view this shows as a decrease in material stiffness, strength and ductility. An intuitive way to describe this is from a microscopical point of view, in terms of effective resisting area in relation to the initial cross-sectional area. As the effective area is reduced and the damage increases, the stress will reduce and the material softens. When the effective area is reduced to zero, the material fails. The evolution of damage can then be expressed in terms of a damage variable D which is expressed by Lemaitre [34] as

$$D = 1 - \frac{A_{effective}}{A_{initial}} \tag{61}$$

where D is the damage variable, $A_{effective}$ is the effective resisting area and $A_{initial}$ is the initial cross-sectional area. The damage can be coupled to the stress according to

$$\sigma^* = \sigma(1 - D) \tag{62}$$

where σ^* is the stress coupled to the damage and σ is the current stress.

2.7.3 Johnson-Cook damage model

The Johnson-Cook damage model is another phenomenological damage model that considers stress triaxiality, strain rate and temperature dependence in the fracture formulation. It is presented here due to its relevance to the damage evolution in GISSMO. The Johnson-Cook damage model uses a linear damage accumulation expressed as

$$D = \frac{\varepsilon_p}{\varepsilon_f} \tag{63}$$

where the fracture strain ε_f is expressed by [35] as

$$\varepsilon_f = (d_1 + d_2 \exp(-d_3\eta)) \left[1 + d_4 ln\left(\frac{\dot{\varepsilon}_e^p}{\dot{\varepsilon}}\right)\right] \tag{64}$$

where d_1, d_2, d_3 and d_4 are material constants. As can be seen in equation (64), the fracture strain is defined as a function of stress triaxiality. As shown by [10], [11] and others, material damage is not only dependent on the triaxiality but also the Lode angle parameter which is why the Johnson-Cook damage model loses its relevance in damage modelling. The fracture strain dependence on triaxiality and independence of the Lode angle parameter in the Johnson-Cook model is illustrated in figure 15.

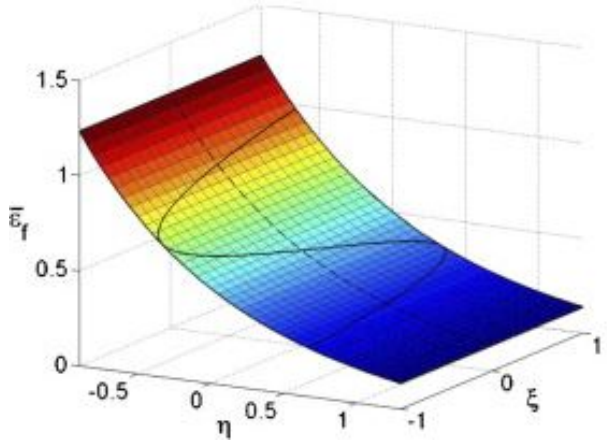

Figure 15: Fracture locus independent of normalized third stress invariant ξ, proposed by Johnson-Cook [11].

2.7.4 GISSMO

The damage accumulation in GISSMO is of Johnson-Cook type, which can be seen in the formulation of the damage evolution described below

$$D = \left(\frac{\varepsilon_p}{\varepsilon_f}\right)^n \tag{65}$$

where ε_p is the plastic strain, ε_f is the fracture strain at a given triaxiality and Lode angle parameter value and n is the non-linear damage exponent. This can be compared to the Johnson-Cook model where the damage accumulation is linear and $n = 1$. If a load path is of varying triaxiality it is necessary with an incremental damage equation (65) can be expressed incrementally as

$$dD = \frac{n}{\varepsilon_f(\eta, \xi)} D^{\frac{n-1}{n}} d\varepsilon^p = f(D, \varepsilon_f) d\varepsilon^p \tag{66}$$

meaning that the damage starts to evolve at the point of initial plastic deformation. The fracture strain in GISSMO, as opposed to the Johnson-Cook model, is dependent on both triaxiality and Lode angle parameter and is constant for every stress state.

The stress is coupled to the damage at the point of material instability which is dependent on effective plastic strain as a function of triaxiality. The variable F determines the point of material instability which evolves with plastic strain as

$$dF = \frac{n}{\varepsilon_i(\eta)} F^{(1-\frac{1}{n})} d\varepsilon^p \qquad 0 \leq F \leq 1 \tag{67}$$

At the point of initial plastic deformation, both the damage and the material instability begin to evolve. The instability parameter F is zero at initial plastic strain and one at the point of necking. The damage parameter is equal to zero at initial plastic strain and reaches a critical value $D_{CRIT} \neq 0$ at the point of necking, which is when the damage is coupled to the stress and material degradation is initiated. At $D = 1$ the material fractures. Beyond the point of instability the stress is coupled to the damage as

$$\sigma^* = \sigma \left[1 - \left(\frac{D - D_{CRIT}}{1 - D_{CRIT}} \right)^{FADEXP} \right] \tag{68}$$

where the fading exponent, $FADEXP$, is a parameter that impacts the softening behavior once the damage has been coupled to the stress. GISSMO is activated in LS-DYNA using *MAT_ADD_DAMAGE_GISSMO [36].

GISSMO can be compared to other damage models, such as the previously mentioned Johnson-Cook and Gurson damage models. The difference in damage accumulation between the Johnson-Cook, Gurson and GISSMO damage models is illustrated in figure 16. It can be observed that, compared to the GISSMO model, the Johnson-Cook model tends to overestimate damage accumulation and the Gurson model underestimates damage due to its inability to consider shear deformation.

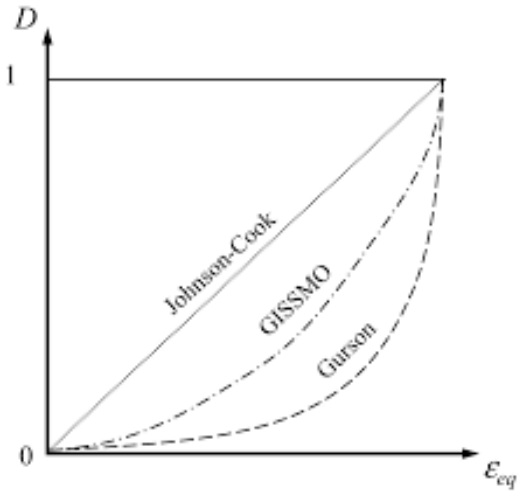

Figure 16: Comparison of damage accumulation between the Johnson-Cook, GISSMO, and the Gurson damage models [37].

2.7.5 Modified Mohr-Coulomb fracture criterion

The Mohr-Coulomb fracture criterion (MMC) is a fracture criterion that has proven to accurately take the effects of Lode angle parameter and triaxiality into account. It was first developed for rock and soil materials and due to the stress state being dependent on the same parameters, the criterion can also be used in ductile metals. The authors of [38] suggested an extension to the Mohr-Coulomb fracture criterion. Their suggestion, the modified Mohr-Coulomb fracture criterion, is used in this work and will be briefly described in this section and a more detailed derivation can be found in their original paper.

The fracture in the Mohr-Coulomb criterion occurs when the normal stress, σ_n and the shear stress, τ reach a critical value defined as

$$(\tau + c_1\sigma_n)_f = c_2 \tag{69}$$

where the parameters c_1 and c_2 are material constants, referred to as a friction coefficient and a shear resistance, respectively.

To find the point of fracture in equation (69) one must solve the maximum value problem expressed in terms of principal stresses as

$$\left(\sqrt{1-c_1^2}+c_1\right)\sigma_1 - \left(\sqrt{1+c_1^2}-1\right)\sigma_3 = 2c_2 \tag{70}$$

In order to express the fracture criterion in the stress space of $(\overline{\varepsilon}_f, \eta, \overline{\theta})$, the principal stresses must be expressed in terms of the spherical coordinate system (σ_m, η, θ). From a geometrical representation of the principal stresses and the deviatoric stresses on the deviatoric plane, the principal stresses can be expressed in terms of σ_m, η and θ as

$$\begin{aligned}\sigma_1 &= \left[1 + \frac{2cos\overline{\theta}}{3\eta}\right]\sigma_m \\ \sigma_2 &= \left[1 + \frac{2cos(\frac{2}{3}\pi + \overline{\theta})}{3\eta}\right]\sigma_m \\ \sigma_3 &= \left[1 + \frac{2cos(\frac{4}{3}\pi + \overline{\theta})}{3\eta}\right]\sigma_m\end{aligned} \tag{71}$$

By inserting equation (71) into equation (70) the Mohr-Coulomb criterion can be expressed in terms of $\overline{\sigma}$, η and θ as

$$\overline{\sigma} = c_2\left[\sqrt{\frac{1+c_1^2}{3}}cos(\frac{\pi}{6} - \overline{\theta}) + c_1\left(\eta + \frac{1}{3}sin(\frac{\pi}{6} - \overline{\theta})\right)\right]^{-1} \tag{72}$$

The same authors proposed a hardening rule dependent on both hydrostatic pressure and Lode angle parameter as

$$\overline{\sigma} = K\overline{\varepsilon}^n[c_\theta^s + (c_\theta^{ax} - c_\theta^s)\frac{\sqrt{3}}{2-\sqrt{3}}\left[sec\left(\frac{\overline{\theta}\pi}{6}\right) - 1\right] \tag{73}$$

$$c_\theta^{ax} = \begin{cases} 1 & \text{for } \overline{\theta} \geq 0 \\ c_\theta^c & \text{for } \overline{\theta} < 0 \end{cases} \tag{74}$$

where K and n are obtained from the power hardening of the material and c_θ^s and c_θ^c describe the pressure and Lode angle dependence. Now the fracture locus of a general 3D-case can be expressed in terms of $\overline{\varepsilon}_f$, η and $\overline{\theta}$ by substituting equation (73) into equation (72) to obtain

$$\begin{aligned}\overline{\varepsilon}_f = \Bigg[&\frac{K}{c_2}\left[c_\theta^s + \frac{\sqrt{3}}{2-\sqrt{3}}(c_\theta^{ax} - c_\theta^s)\left(sec\left(\frac{\overline{\theta}\pi}{6}\right) - 1\right)\right] \\ &\left[\sqrt{\frac{1+c_1^2}{3}}cos\left(\frac{\overline{\theta}\pi}{6}\right) + c_1\left(\eta + \frac{1}{3}sin\left(\frac{\overline{\theta}\pi}{6}\right)\right)\right]\Bigg]^{-\frac{1}{n}}\end{aligned} \tag{75}$$

In equation (75) there are six parameters $(K, n, c_\theta^s, c_\theta^c, c_1, c_2)$ that need to be determined. K and n are determined using experimental data, c_θ^c is set to one while the other three parameters are determined by fitting a surface to experimental fracture points. In figure 17, a hypothetical fracture locus using the modified Mohr-Coulomb fracture criterion is used.

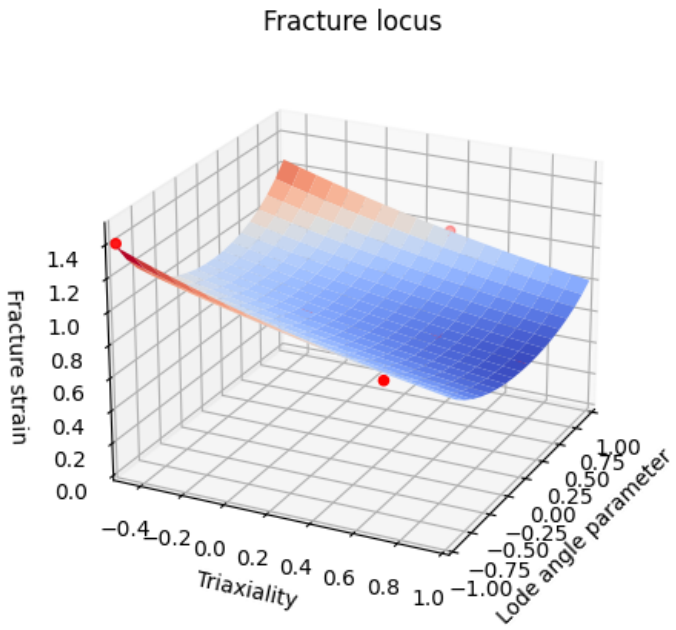

Figure 17: An illustration of a hypothetical fracture locus, indicated by the red dots, using the modified Mohr-Coulomb fracture criterion.

3 Method

To develop a damage model several steps need to be performed. Firstly, relevant experimental data is gathered as presented in section 2.4, followed by numerical modelling of the test specimens. Thereafter, the material model is calibrated and the damage parameters are determined. Once the damage parameters are determined the fracture locus is obtained which is followed by a mesh regularization.

3.1 Numerical setup

In this section the numerical modelling of the material model and the damage model calibration is presented. The numerical setup for a punching model is also presented as it is used to test the damage model in a practical case even though it cannot be validated with measured test data.

3.1.1 Meshing and boundary conditions

The specimens are modelled using solid elements with reduced integration. In the case of a plane stress problem shell elements can be used but due to the three-dimensionality of the punching process, solid elements are necessesary to describe the different stress states. As opposed to the pre-necking state, the damage model is element size dependent. Due to this, the element size used in the future application of the damage model should also be the element size used in the damage model calibration. As the damage model is to be applied to forming simulations with an element length as short as 0.1 mm, the same element length should be used in the damage model calibration as well. However, due to computational limitations and lack of time, an element length of 0.125 mm is used. Only the part of the specimen that is affected by the damage model, i.e. the part that experiences large enough plastic strains, has a refined mesh where the damage model is active. It is possible to do a mesh regularization, meaning that the resulting damage can be scaled based on element size which is a method of making finite element models mesh independent.

If possible, symmetry conditions are used for the models such as for the uniaxial tensile test which is modelled as an eighth of the original model as can be seen in figure 18. Symmetry conditions are used along the bottom boundary in the Y-direction, along the left boundary in the X-direction and along the thickness in the Z-direction. This greatly reduces the size of the model and therefore also the computational time. As can be seen when comparing the two models for the uniaxial tensile test, the upper portion has been removed as that section is clamped in the experimental setup. The force is measured using a cross section plane and the displacement is measured using a history node located in the clamped section.

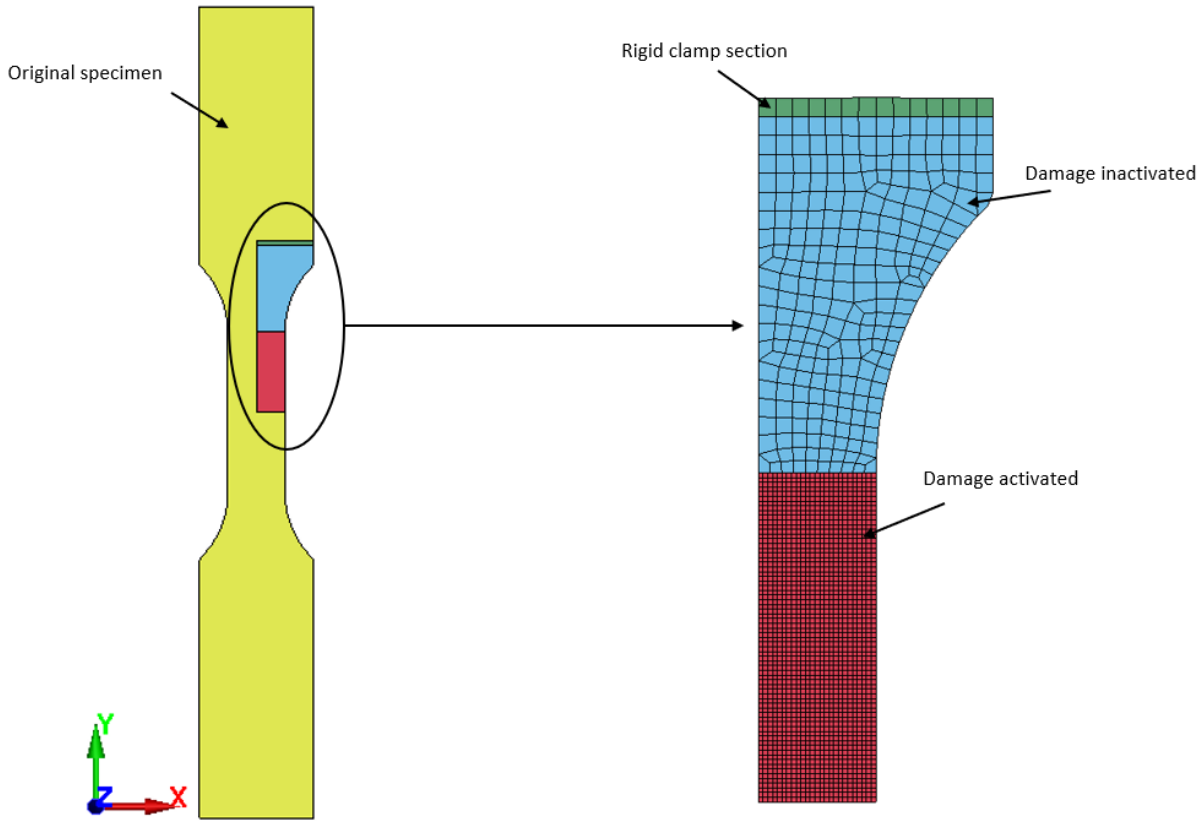

Figure 18: Original and symmetric model of the uniaxial tensile test.

3.1.2 Sensitivity study

A sensitivity study is conducted for the uniaxial tensile test to reduce simulation time while assuring mesh independence in the material model calibration. Both the mesh and the element type are considered in the sensitivity study. For the mesh study, three different element sizes are compared, as presented in table 1. The resulting three hardening curves are presented in figure 19.

Table 1: Meshing parameters for the uniaxial tensile test.

Model	a	b	c
Maximum length	0.1 mm	0.3 mm	0.5 mm
Minimum length	0.1 mm	0.3 mm	0.5 mm
Number of elements	24000	3500	1500
CPU time	2h 03 min	23 min	12 min

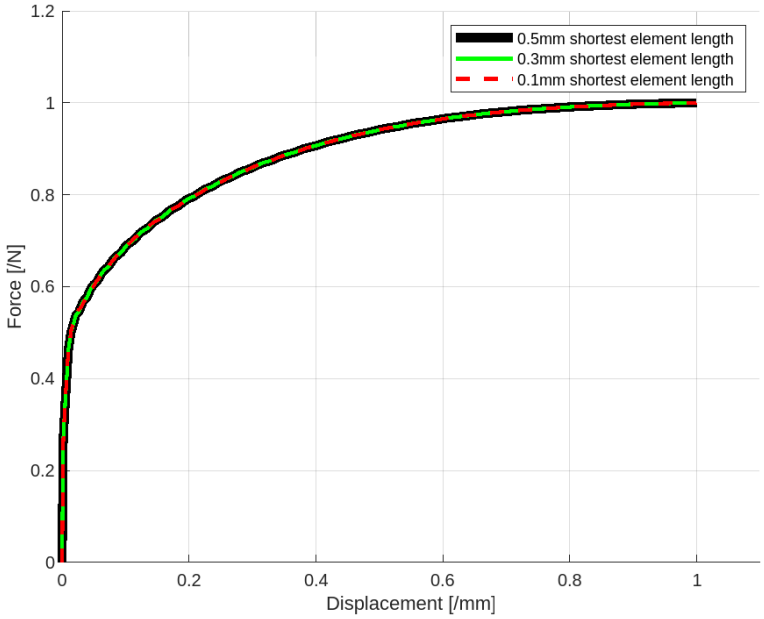

Figure 19: Resulting hardening curves for different element lengths.

Another way to reduce computational time is to reduce the number of integration points in each element. The force-displacement response for fully integrated elements with eight integration points is compared with the response for under-integrated elements with one integration point. In figure 20 the force-displacement response for the uniaxial tensile test is illustrated.

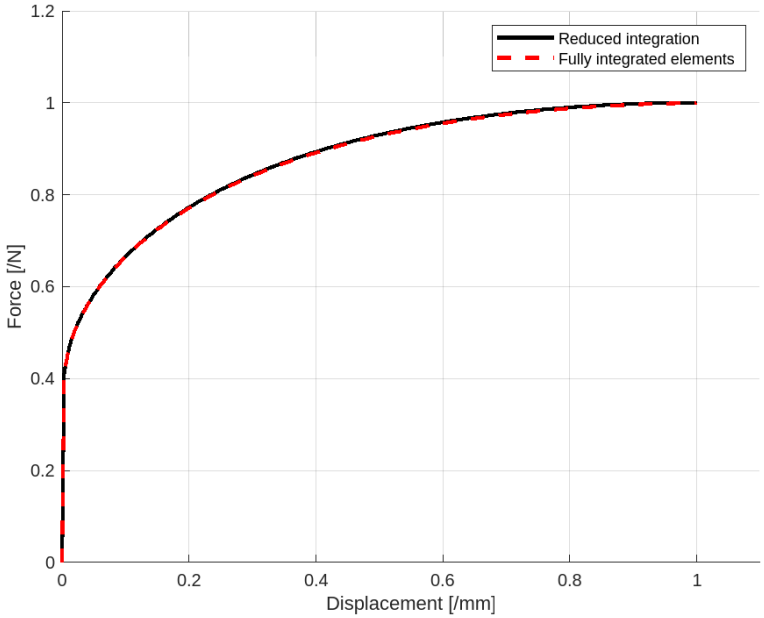

Figure 20: Force-displacement response for fully integrated and under-integrated solid elements.

3.1.3 Forming simulation with a punch

To test the damage model in a practical case, a forming simulation including a punch is set up. The forming model has a stamp and a die with a 0.5 mm blank in between as illustrated in figure 21 below. The stamp and die are modelled as rigid shell bodies while the blank is of 316 stainless steel modelled with solid elements. The forming simulation is run both using the original calibration element size and the smaller element size with regularization.

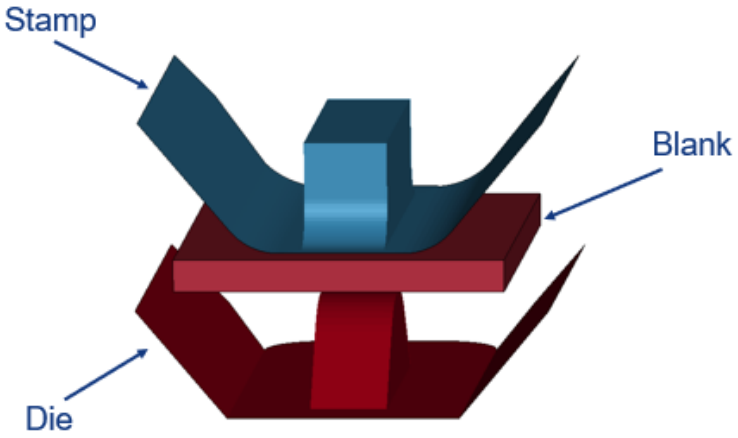

Figure 21: Forming model with a punch.

3.2 Calibration of material model

The material model is used to describe the material behaviour until the point of necking and is calibrated using experimental data which is done by determining a hardening curve based on a tensile test. The tensile test used to calibrate the hardening curve is the uniaxial tensile test presented in section 2.4.1. In this section the method of calibrating the material model will be described.

3.2.1 Material hardening

Once the material is stretched beyond the elastic limit, i.e. the yield strength, it starts to experience plastic deformation. The yield stress is assumed to be at 0.2% plastic strain, which is a common way to determine the yield stress of a material. The hardening curve is determined by fitting a curve to the experimental stress-strain data. The curve fitting is done in Excel using the least-squares method which is described in section 2.4.7. The data used for the curve fitting is every measured experimental point from the yield stress until the point of necking. The hardening behavior of the material is represented by a power law model, defined as $\sigma = K\varepsilon^n$, which is determined using experimental data from the uniaxial tensile test. In the power law, K is a material constant and n is the strain hardening exponent. In figure 22 the experimental true stress as a function of plastic strain for the

uniaxial tensile test is presented together with the fitted hardening curve. The hardening curve is validated using the four experimental tests cases, namely the uniaxial tensile test, the shear test, the plane strain test and the biaxial bulge test, which were presented in section 2.4. The hardening curve is directly used in the material model in LS-DYNA as a load curve consisting of the true stress values at given plastic strains. The points on the hardening curve beyond the necking point are extrapolated stress values that are coupled to the damage as previously described.

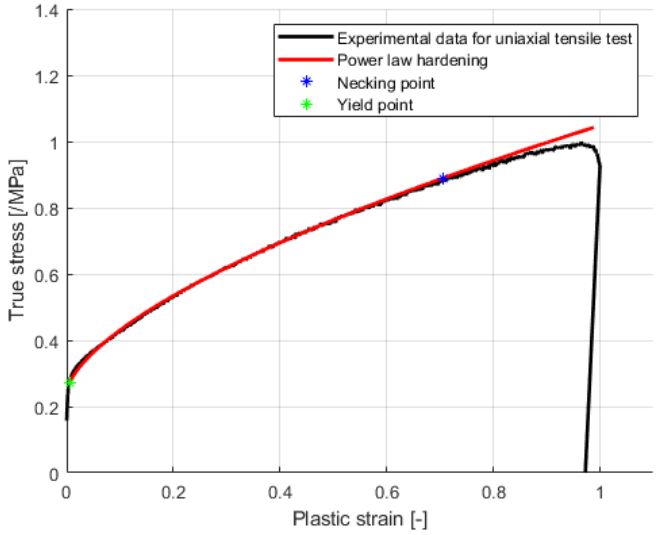

Figure 22: Hardening curve fitted using a power law.

3.2.2 Anisotropic behavior

As mentioned in section 2.4.6, the rolled 316 stainless steel has shown anisotropic behaviour in previous tests, which is described in the material model by parameters defining the yield stress in different directions together with the R-values. The material properties for the 316 stainless steel used in the tests will not be presented here due to confidentiality.

3.3 Damage modelling

To model damage and failure using GISSMO, a number of input parameters are required as presented in section 2.7.4. These parameters affect the onset of necking and the post necking behaviour. The damage and fracture are dependent on the stress state of the material which is described in the Lode angle parameter and triaxiality stress space. Depending on the stress state, the material will have different points of instability onset and fracture strain and to obtain these values, the simulation data is recorded as force and displacement and is matched against experimental data.

3.3.1 Parameter identification

The software LS-OPT is used for parameter identification of the parametrized finite element models. The parameters that are determined are the damage exponent, the fading exponent, the instability strain and the fracture strain using the least square method with experimental fitting data. In figure 23 the user interface in LS-OPT is illustrated where an example parameter setup is also shown. The variables $e1$, $e2$ and $e3$ represent instability strains and $f1$, $f2$ and $f3$ represent the fracture strains at different values of triaxiality. The parameters $fadexp$ and $dmgexp$ represent the fading exponent and the damage exponent, respectively, which were introduced in section 2.7.4.

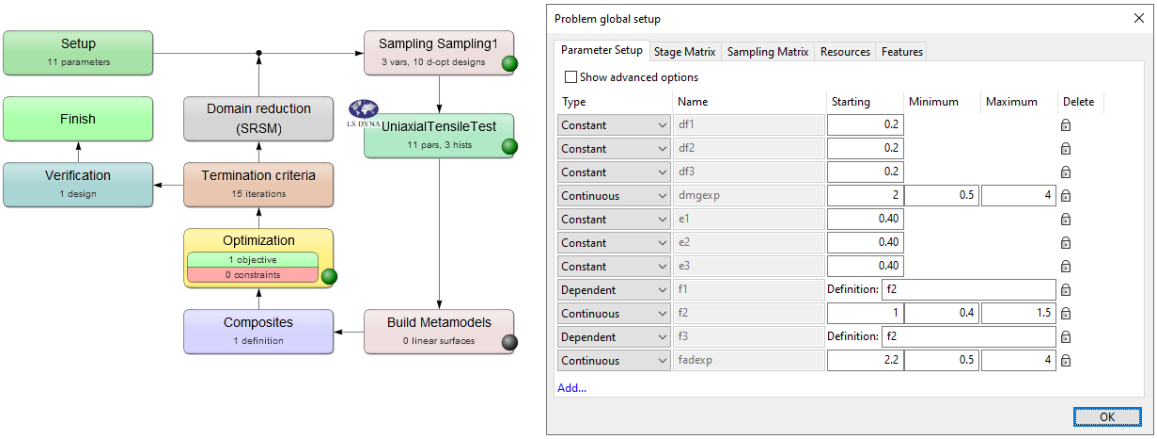

Figure 23: LS-OPT user interface for parameter identification.

Each of the models is run independently in LS-OPT to determine start values for their respective triaxiality values and thereafter the obtained parameter values are combined into one general GISSMO-card in LS-DYNA and tested for each model. The stress state for each model is measured from DIC data as an average value obtained from the center region of each specimen, which is presented in table 2.

Table 2: Stress state for each model.

Case	Triaxiality, η	Lode angle parameter, θ
Shear	0.100	0
Uniaxial tension	0.333	1
Plane strain	0.577	0
Biaxial tension	0.677	-1

Depending on the result, i.e. if further parameter fitting is necessary, a complete optimization with all models running simultaneously can be carried out. In the individual runs the strain values are independent of triaxiality which is necessary to make them independent of the order of fitting. Furthermore, the Lode angle parameter is not taken into account in the parameter optimization which could potentially pose a problem if different tests show similar

triaxialities but different Lode angle parameters, i.e. the plane stress assumption may not be enough to describe the stress state. In figure 24 an example of an initial instability- and fracture strain setup for the uniaxial tensile test is illustrated. The instability strain for the uniaxial tensile test is taken directly from the experimental data as the equivalent plastic strain at maximum stress. For the other tests this value is determined using LS-OPT.

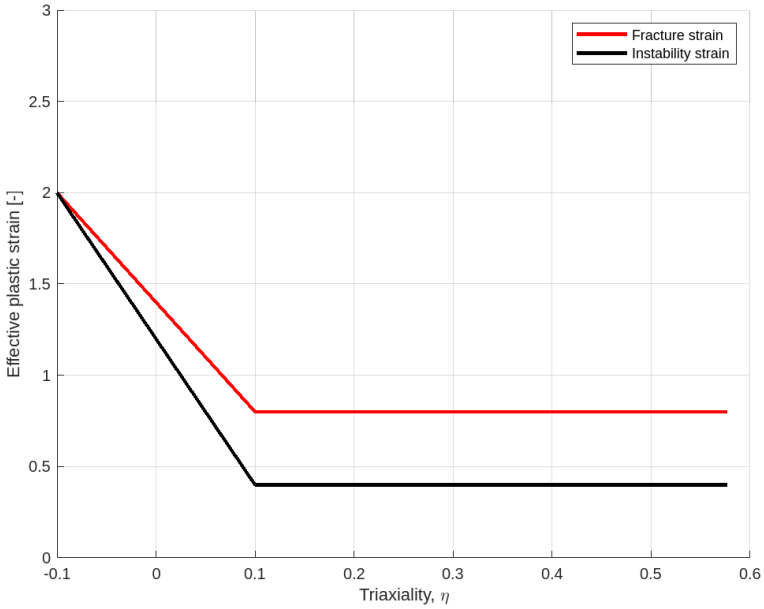

Figure 24: Example setup for an LS-OPT parameter optimization.

The points used for curve fitting in the algorithm are presented in figure 25 together with the experimental data. Only points from the softening of the experimental data are used as this is where the damage model acts and the stress is coupled to the material model. In order to save time in LS-OPT, the number of points should be as low as possible while still describing the softening behavior.

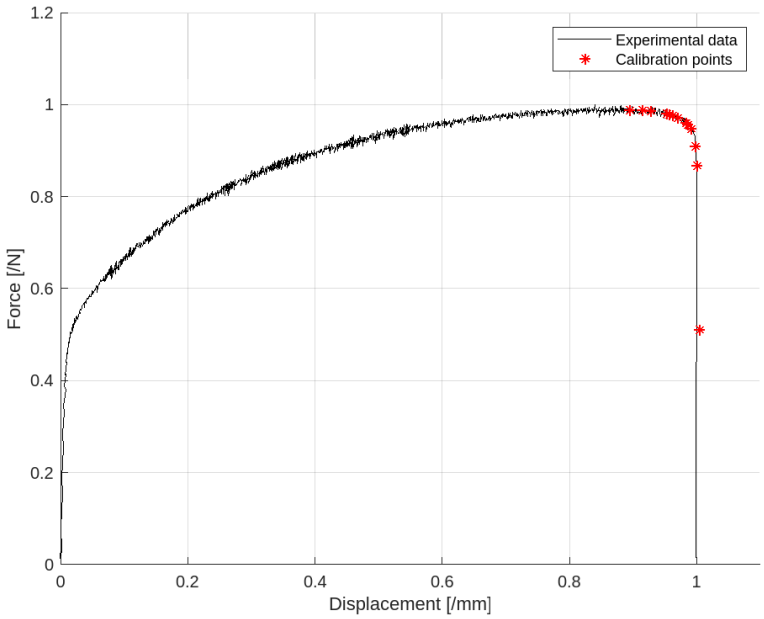

Figure 25: Experimental data with chosen damage calibration points.

3.3.2 Fracture locus

The fracture locus is formed by the fracture criterion based on the fracture strains found in the different stress states. Due to the vast number of stress states it is not possible to find the fracture strain for every load case. However, it is possible to find the fracture strain for stress states that describe the general shape of the fracture locus, hence the different experiments that were conducted. Certain assumptions must still be made, such as the fracture criterion, which in this case is chosen as the modified Mohr-Coloumb criterion described in section 2.7.5. To create the fracture locus, a number of points corresponding to measured fracture strains, obtained using LS-OPT, are used in a python script in which a curvefit function generates a surface according to the fracture criterion. The points that make up the surface are written to an input file as load curves in a table that can be used in LS-DYNA using the *INCLUDE keyword. An example of a fracture locus is illustrated in figure 17.

3.3.3 Mesh regularization

Due to the mesh dependency of the damage model it should be calibrated using the same element size as for the case to which it is applied. Due to long computational times the element size used in the damage model calibration is larger than the size for the intended purpose. In order to make the solution mesh independent a mesh regularization is conducted, meaning that a scale factor for the fracture strain is used. To find the scale factor, the uniaxial tensile test is used with an element length of 0.1 mm and the resulting force-displacement curve is compared to the original model with an element length of 0.125 mm.

From this a scale factor for the fracture strain is guessed and tested for the 0.1 mm case. Once the scale factor has been obtained it is tested with the other models.

4 Results

In this section the results for the material model and the damage model are presented separately. Furthermore, comparisons with experimental data are presented as well as the results from the forming simulation with a punch with and without mesh regularization.

4.1 Material model calibration

The resulting hardening behaviour for the Barlat-YLD2000 material model is presented for each model in this section. No damage is activated when validating the material model.

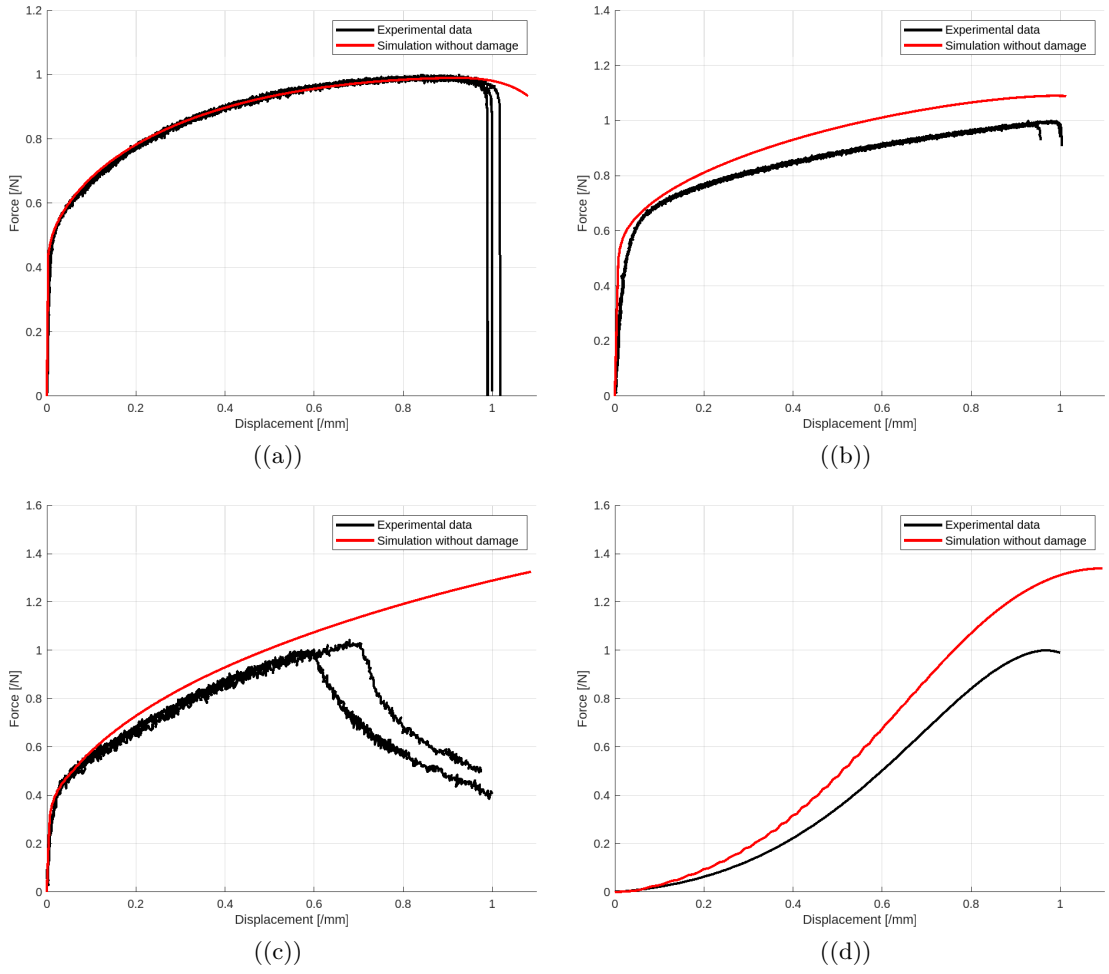

Figure 26: Experimental data and simulated response from the ((a)) uniaxial tensile test, ((b)) plane strain test, ((c)) shear stress test and ((d)) biaxial bulge test without an active damage model.

4.2 Damage parameter identification

The results from the GISSMO parameter identification using LS-OPT are presented in this section.

Table 3: Resulting parameters from LS-OPT.

Case	Damage exponent	Fading exponent	Instability strain, ε_i	Fracture strain, ε_f
Shear	2.28	2.3	0.51	0.66
Uniaxial tension	2.28	2.3	0.296	0.67
Plane strain	2.28	2.3	0.26	0.78
Biaxial tension	2.28	2.3	0.31	0.73

In figure 27 the result for each model is presented. The damage parameters obtained in LS-OPT are used for each individual case independent of each other.

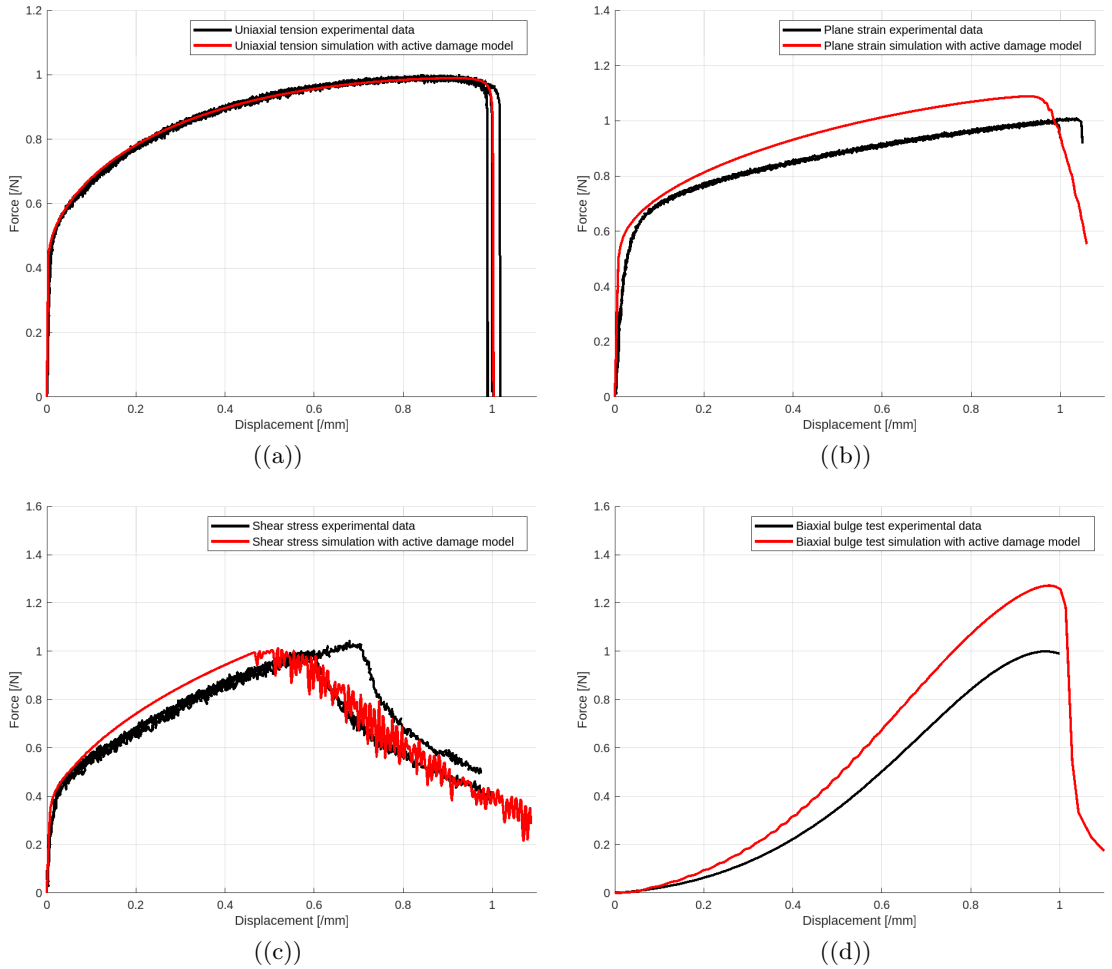

Figure 27: Experimental data and simulated response from the ((a)) uniaxial tensile test ((b)) plane strain test, ((c)) shear stress test and ((d)) biaxial bulge test with damage parameters obtained from LS-OPT for each case.

4.2.1 Combined GISSMO material card

In figure 28 the result from each individual case is presented when the damage parameters obtained in LS-OPT are combined into one material card in LS-DYNA.

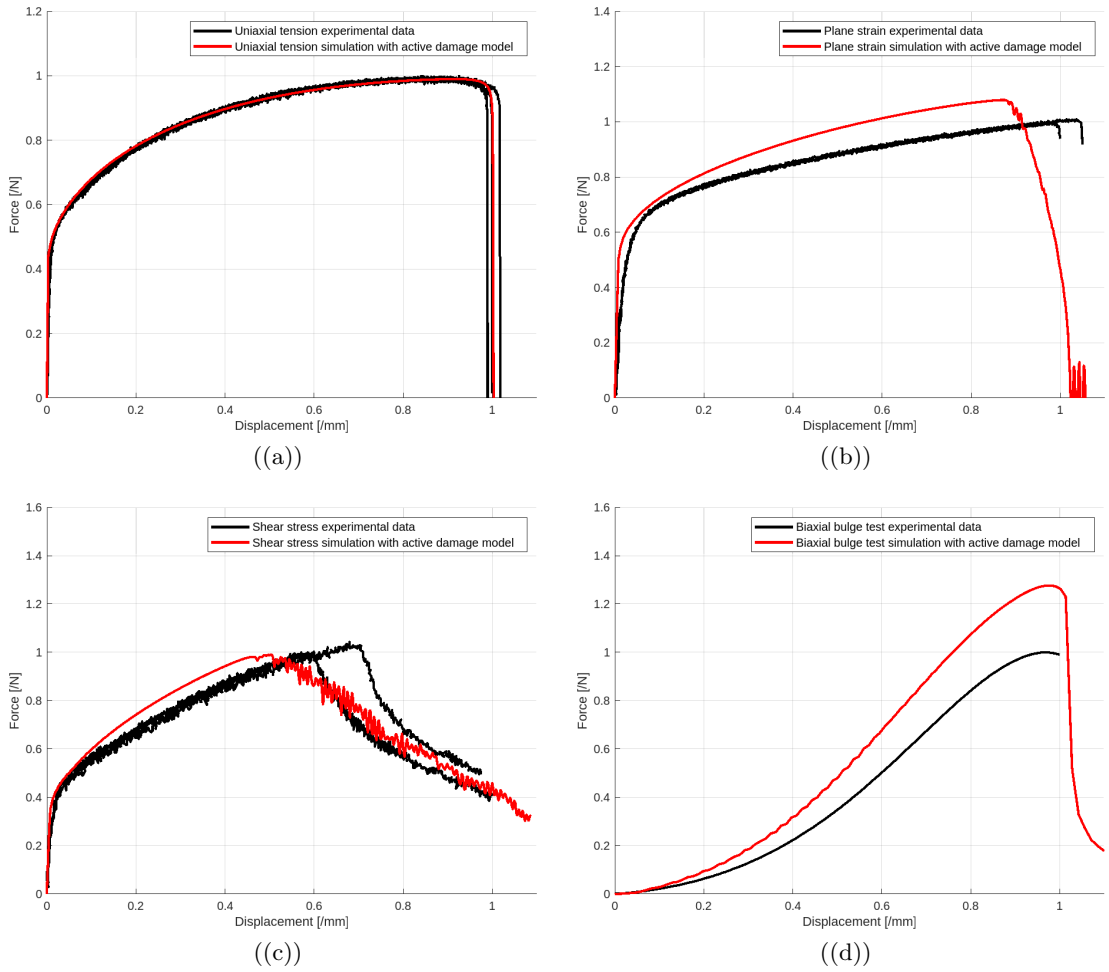

Figure 28: Experimental data and simulated response from the ((a)) uniaxial tensile test ((b)) plane strain test, ((c)) shear stress test and ((d)) biaxial bulge test with damage parameters combined into one card in LS-DYNA.

4.2.2 Uniaxial tensile test

The stress state for the uniaxial tensile test prior to fracture is illustrated in figure 29 which shows a uniform distribution of its theoretical stress state value.

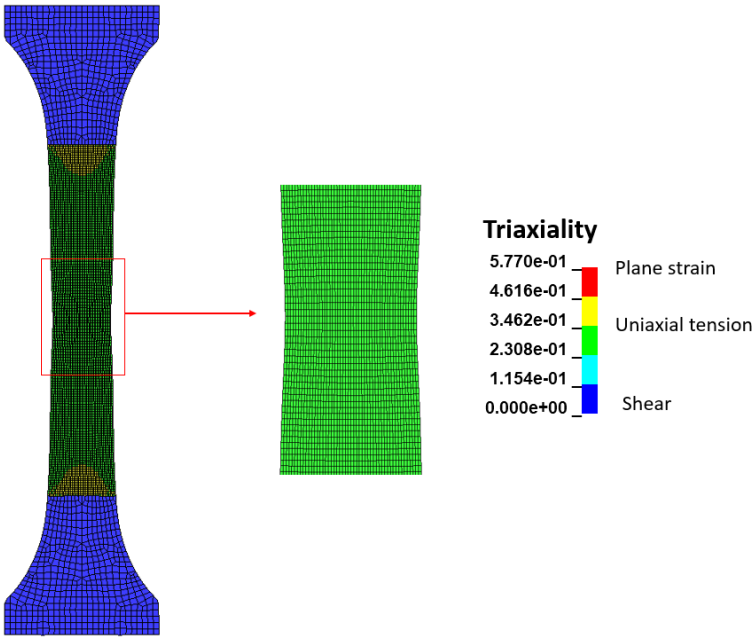

Figure 29: Visualization of stress state in uniaxial tension model prior to fracture initiation.

4.2.3 Plane strain test

The stress state for the plane strain test prior to fracture is illustrated in figure 30 shows a non-uniform stress state and the fracture is not initiated in its theoretical plain strain stress state.

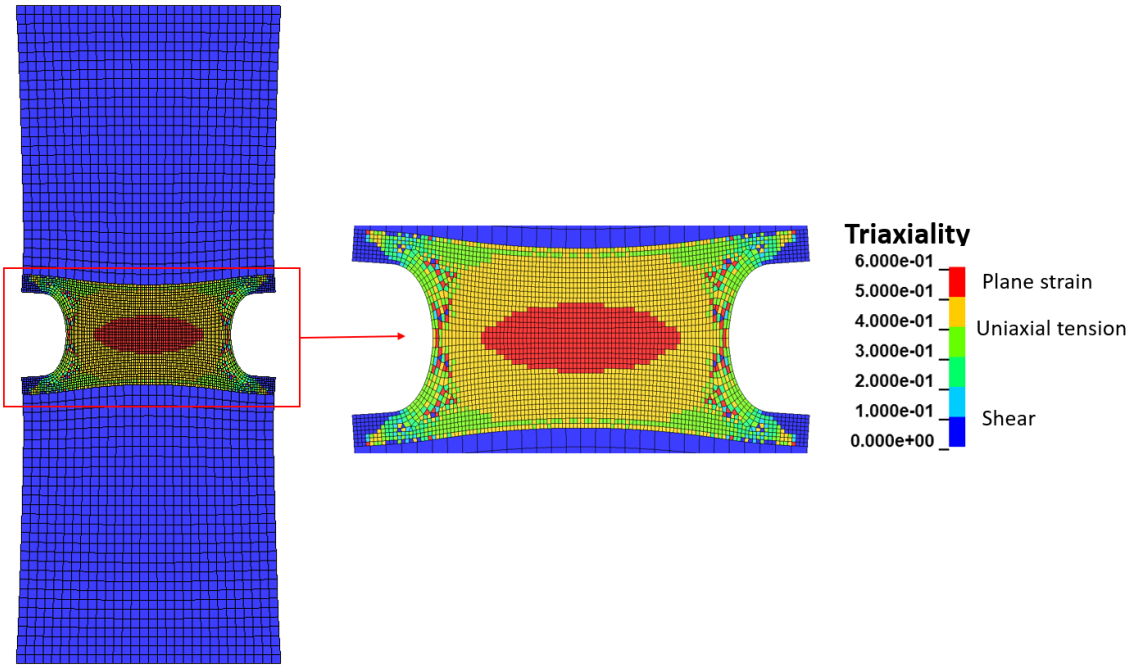

Figure 30: Visualization of stress state in the plane strain model prior to fracture initiation.

In figure 31 the strain field distribution from the plane strain experiment obtained using DIC is illustrated. A part of it has been cropped off and compared to the simulated strain field distribution in figure 32. It can be seen that the strain distribution is similar between the two.

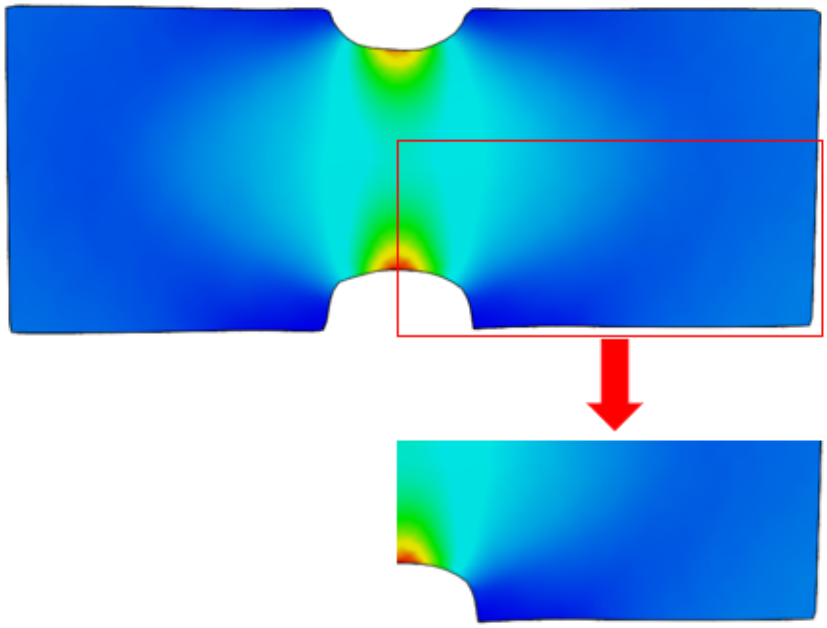

Figure 31: Experimental strain field distribution in the plane strain model prior to fracture initiation.

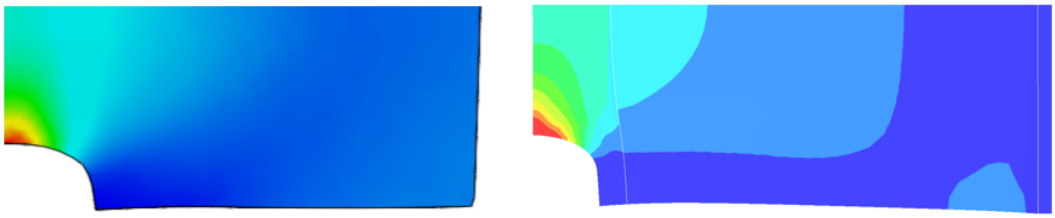

((a)) ((b))

Figure 32: Strain field distribution in the plane strain model from ((a)) experimental DIC data and ((b)) simulated response.

4.2.4 Shear stress test

The stress state for the shear stress after fracture is presented in figure 33 and it can be seen that the fracture occurs in a stress state close to uniaxial tension and not in its theoretical shear stress state.

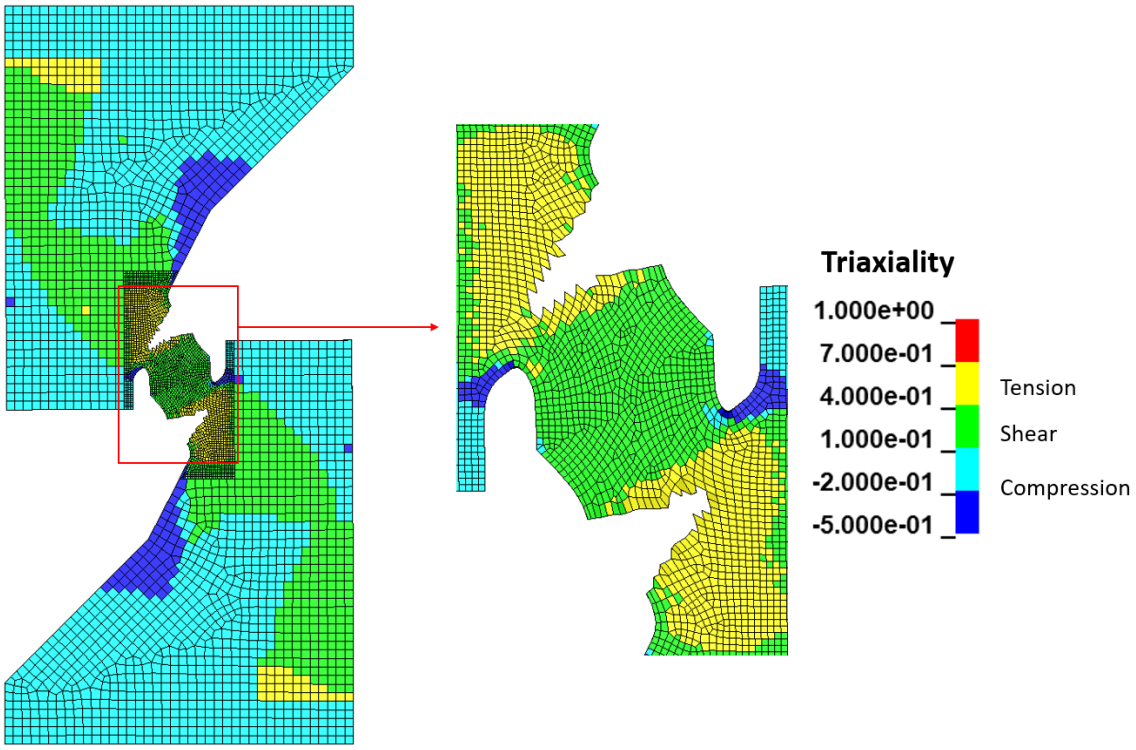

Figure 33: Visualization of stress state in the shear stress model after fracture initiation and propagation.

4.2.5 Biaxial bulge test

The strain distribution of the biaxial bulge test is strongly influenced by the friction between the sheet metal and the hemispherical punch, and the simulation results are in good agreement with the experimental data obtained from DIC. In figure 34 the strain distribution for the biaxial bulge test is illustrated.

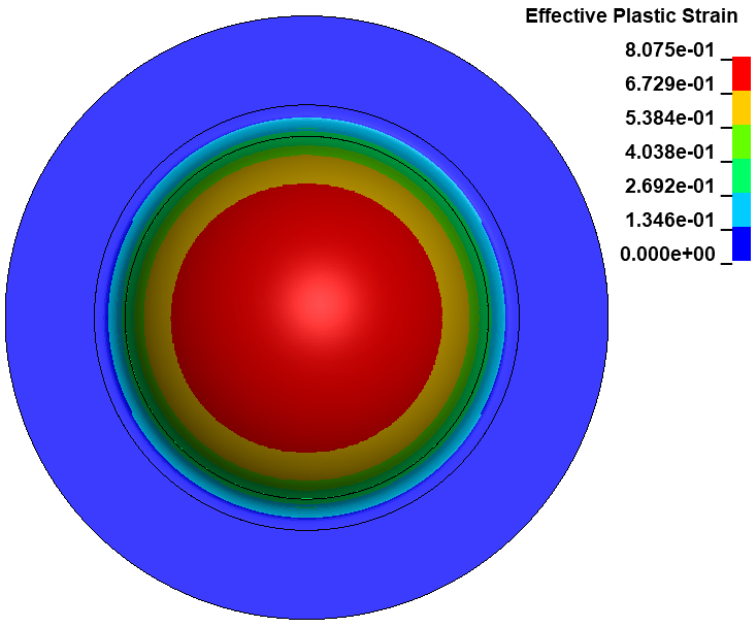

Figure 34: Visualization of the simulated strain field distribution of the biaxial bulge model prior to fracture viewed from above.

In figure 35 the fracture for the biaxial bulge test is illustrated, which emphasizes the issues with the material model.

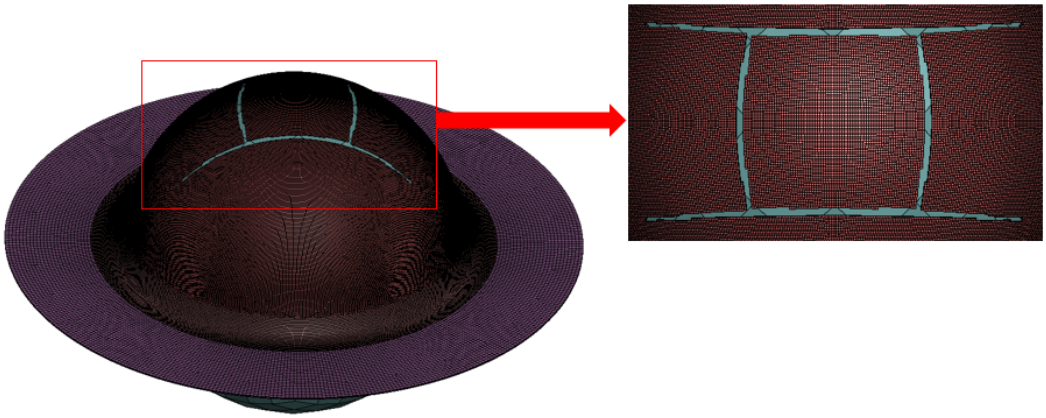

Figure 35: Visualization of fracture in the biaxial bulge model in a perspective view on the left and viewed from above on the right.

4.3 Fracture locus

Due to the observations made in figure 30 and figure 33, some of the parameters in table 3 must be modified before the final fracture strain can take form. The fracture strain for the plane strain model has been modified as well as the instability strain for the shear stress model, both in their theoretical stress states. The results show that the fracture is not

initiated in their respective theoretical stress states which implies that the obtained fracture strain is not applicable in that stress state. Due to this observation, the fracture strain for the plane strain model is approximated to better agree with the MMC fracture criterion. The same is done with the instability strain for the shear stress model. The final fracture strains used to fit the surface are presented in table 4 and the final fracture locus is illustrated in figure 36 where the obtained stress states are compared with the theoretical stress states for the plane strain and shear stress models.

Table 4: Modified parameters from LS-OPT based on simulation observations.

Case	Damage exponent	Fading exponent	Instability strain, ε_i	Fracture strain, ε_f
Shear	2.28	2.3	0.29	0.66
Uniaxial tension	2.28	2.3	0.296	0.67
Plane strain	2.28	2.3	0.26	0.62
Biaxial tension	2.28	2.3	0.31	0.73

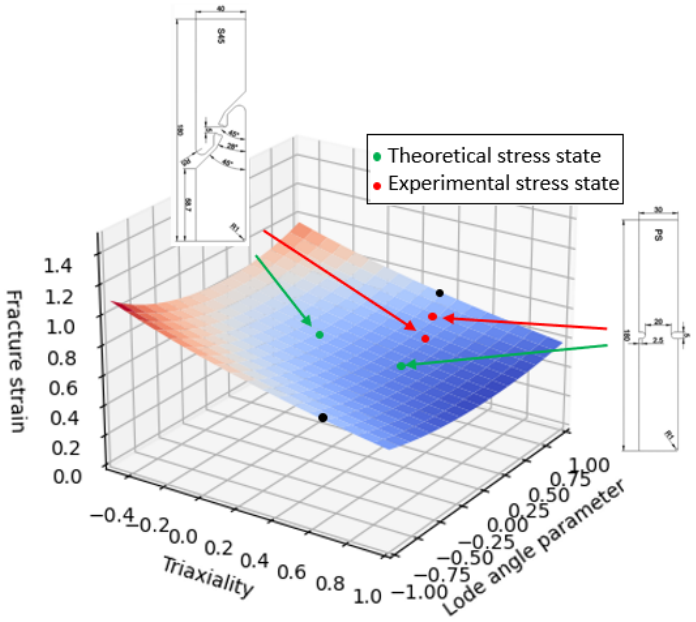

Figure 36: Comparison between theoretical and obtained stress states for the plane strain and shear stress models. The green arrows refer to the desired stress states and the red arrows refer to the stress states obtained in the present experiments.

The final fracture locus used in the damage model is illustrated in figure 37 where no comparison is made between stress states. The stress states used for the surface fitting are represented by the black markers. Due to the lack of experimental data, a point has been added to increase the fracture strain in the compressive stress state. This is based on the fact that the fracture strain has, in previous research, proven to be a monotonically decreasing function of triaxiality and that the model should not be limited in the compressive stress

state. The fracture locus shows good agreement between the final fracture strains and the modified Mohr-Coulomb fracture criterion with an R-squared value of 0.98.

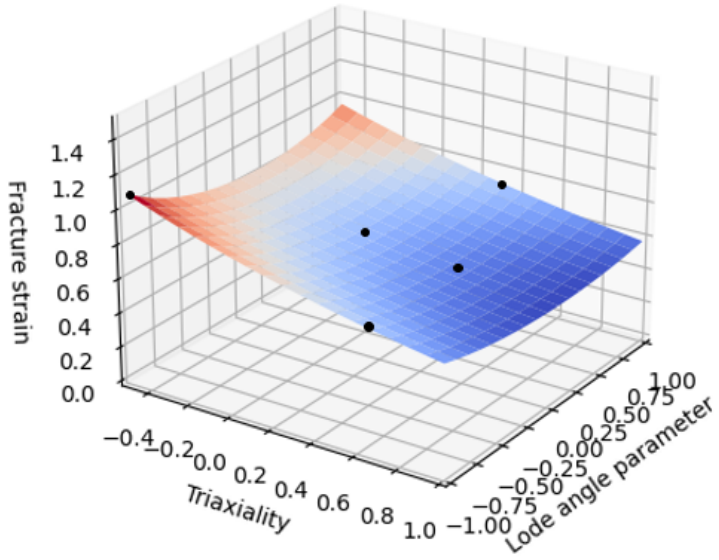

Figure 37: Fracture locus created using the MMC fracture criterion and the fracture strains in table 4.

The fracture strain as a function of triaxiality for the plane stress case is presented in figure 38. The black markers represent the theoretical stress states of the experiments.

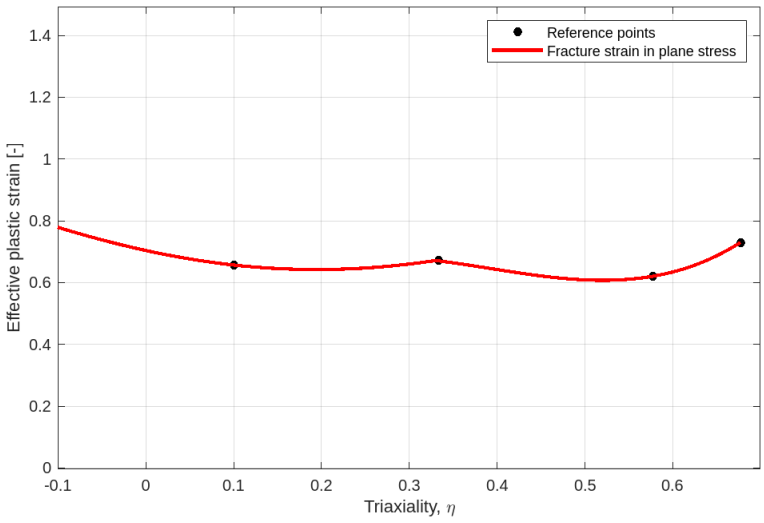

Figure 38: Triaxiality-strain evolution in plane stress.

4.3.1 Experimental models

In this section the results from each model using the fracture locus will be presented.

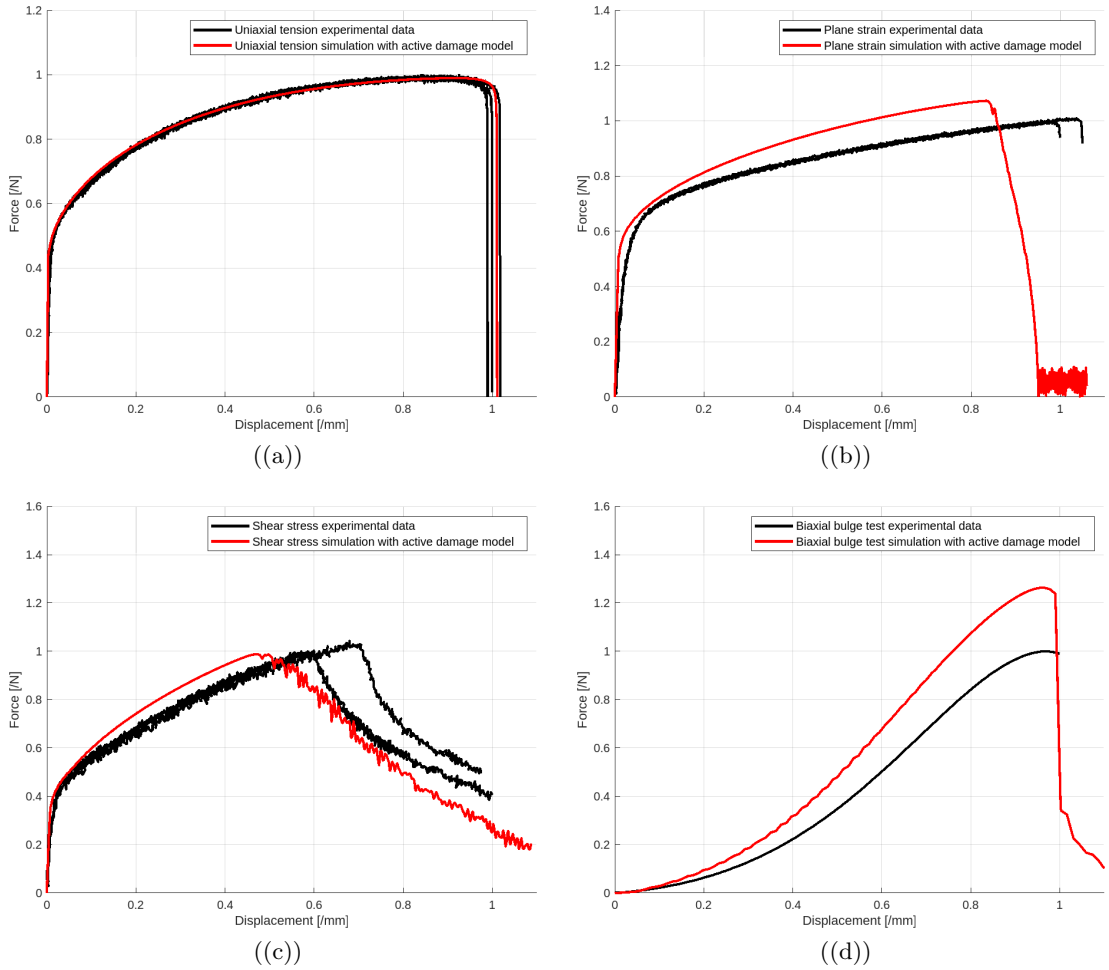

Figure 39: Experimental data and simulated response from the ((a)) uniaxial tensile test ((b)) plane strain test, ((c)) shear stress test and ((d)) biaxial bulge test using the fracture locus presented in figure 37.

4.3.2 Punch model

The results from the forming model with a punch cannot be quantified and compared to experimental data such as the other models. It is possible however, to analyze the results and discuss the feasibility of the simulation. The resulting blank geometry from the forming simulation with a punch using the obtained fracture locus is illustrated in figure 40.

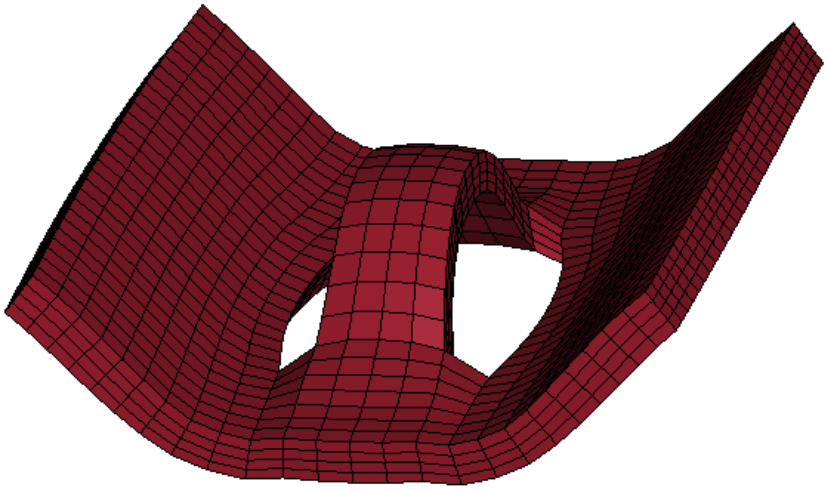

Figure 40: Resulting geometry of forming simulation with a punch.

The stress state in a forming simulation is not uniform and generally varies between a uniaxial tension and a biaxial stress state. When a punch is included however, the stress state in the immediate area around the punch is highly variable, as depicted in figure 41. Due to this, the accuracy of the damage model is clearly dependent on the stress states of the tests that have been performed. The varying stress state in the punching process shows that a plane stress assumption is not accurate and the Lode angle dependence must be accounted for as well as the need for a wide variety of experimental stress states for accurate damage model calibration.

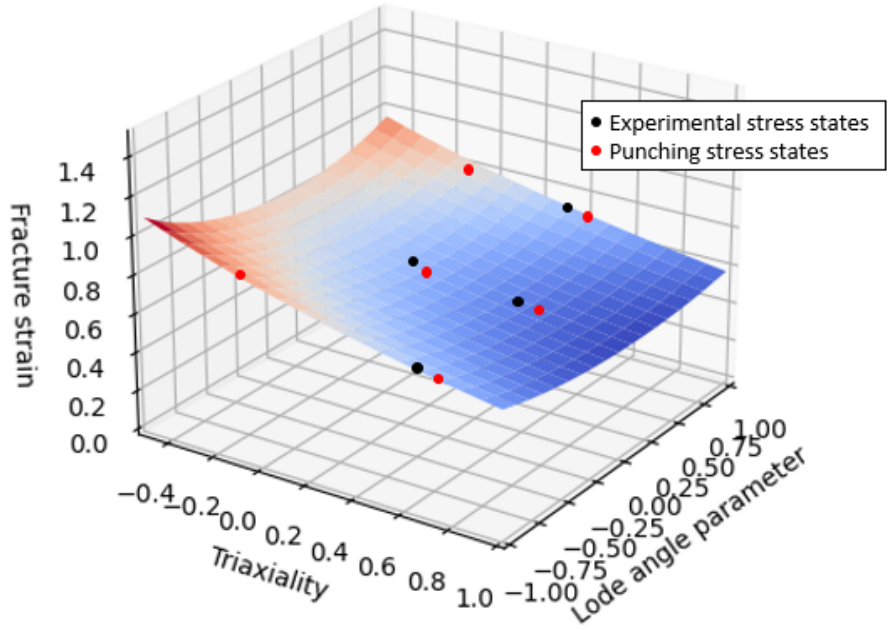

Figure 41: Stress states of a sheet in forming with a punch and the theoretical stress states of the experiments.

4.4 Mesh regularization

The mesh regularization is done for the uniaxial tensile test and then applied on the other models. In this section the regularization results for the uniaxial tensile test and its application on the forming model with a punch are presented. In figure 42 the force displacement response for the uniaxial tensile test with the original element length of 0.125 mm is presented together with the response using an element size of 0.1 mm with and without a regularization factor.

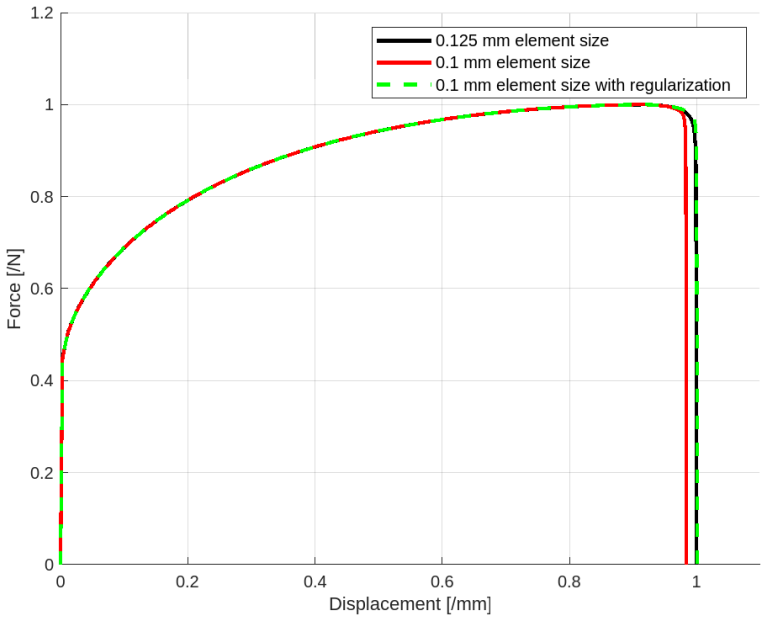

Figure 42: Force displacement response for the uniaxial tensile test with different element lengths and with regularization.

In figure 43 the forming simulation with a punch is illustrated with the original element length of 0.125 mm without a regularization factor and an element length of 0.1 mm with a regularization factor. This illustrates the mesh dependency of the damage model.

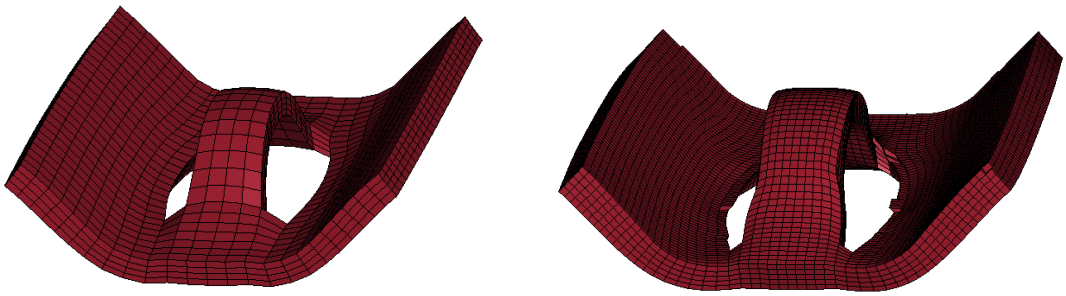

((a)) ((b))

Figure 43: Comparison of the forming simulation with a punch with ((a)) element length of 0.125 mm without a regularization factor and ((b)) element length of 0.1 mm with a regularization factor.

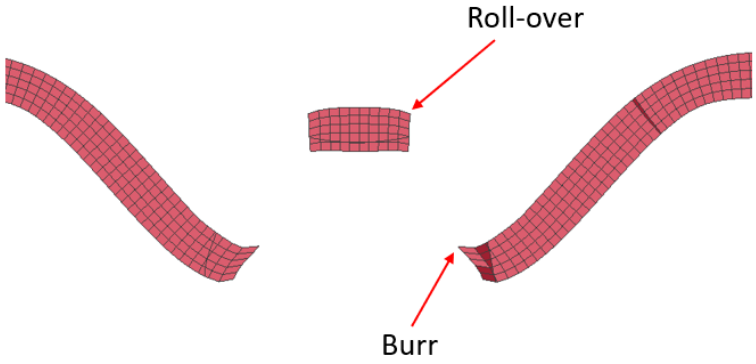

Figure 44: A cross section of the punch where roll-over and burr can be seen.

5 Discussion

In this section, the results will be adressed and possible sources of error will be discussed. Additionally, suggestions for future work will be provided.

5.1 Material model

The material model response, as presented in section 4.1, agrees well the experimental results for the uniaxial tensile test, but for the other tests the response is stiffer than the experimental data. Some inaccuracy is not unexpected, partly because the material model is calibrated based only on the uniaxial tensile test and partly due to the lack of experimental data to accurately assess anisotropy. The inaccuracy of the material model can be seen in figure 35 where the biaxial bulge test fractures unnaturally. Furthermore, the modelling of the biaxial bulge test has inherent problems such as contact and friction conditions. The force displacement response turned out to be especially dependent on the friction between the clamps and the sheet metal. The strain distribution on the metal sheet showed dependency on the friction between the hemispherical bulge and the sheet metal. These issues require information regarding how the experiments were conducted and an accurate estimate of the friction conditions. They should perhaps be avoided altogether by designing the experiment differently.

5.2 Damage model

The stress state in a punching process varies greatly between different stress states which requires a wide variety of stress states in the experimental data to calibrate the damage model. The current experimental data does not include a pure shear or compressive stress state, which exist during the punching process. This suggests that additional experiments that cover the missing stress states should be conducted in order to predict the fracture behaviour during punching.

Instead of obtaining the damage parameters using LS-OPT, a possible approach is to use digital image correlation (DIC) to map the strain field onto a mesh by assigning the displacement and strain values at each node of the mesh. From this, the instability and fracture strains can be obtained and be used to determine the damage parameters. Another potentially accurate but computationally demanding method of obtaining the damage parameters is to parametrize a fracture locus and vary the parameters in LS-OPT in a full-field parameter identification with all four models simultaneously. This would add the Lode angle dependency in the parameter optimization algorithm which could provide a more exact fracture surface.

The use of the MMC fracture criterion assumes that the damage in every stress state can be described by experiments in a plane stress state and therefore also that the fracture

criterion accurately estimates the fracture strains in other stress states. The choice to use the MMC fracture criterion is based on successful results in previous research regarding ductile fracture. The results from this work do not show perfect agreement with the criterion but this is believed to be due to the design of the experiments and the difficulty characterizing the stress states. However, further testing in a wider variety of stress states would be necessary to confirm that the MMC criterion is accurate.

Regarding the regularization, it can be seen in figure 43 that, despite the regularization, the resulting geometries of the punch differ which raises the question of whether the regularization is accurate. The difference between them is due to material draw-in towards the punch when a finer mesh is used. The draw-in found in the punch models with a shorter element length is consistent with previous results at Alfa Laval, while the punch model with a longer element length does not show enough draw-in which may be a modelling issue. Even though the results from the forming simulation with a punch cannot be validated, the model shows a promising result as it has both a burr and a roll-over, which are natural characteristics of a punch. This is illustrated in figure 44.

5.3 Sources of error

The characterization of the stress state of a geometry did not turn out to be a straight forward process. In the uniaxial tensile test the stress state is uniform and the fracture occurs in the theoretical stress state as presented in figure 29. In the plane strain test however, the localized strain in the notch creates a tensile stress state in the critical edge element and not a plane strain stress state as can be seen in figure 30. This results in that the fracture is initiated in a region close to uniaxial tension which raises the question of which stress state the specimen can be considered to be in. The effect of this can be seen when comparing the results from the plane strain test using the individual damage parameters obtained in LS-OPT in figure 27 with the damage parameters combined in one material card in figure 28. It can be observed that the force displacement response differs, which suggests that the fracture of the plane strain test does not occur in its theoretical stress state. This leads to difficulties finding a fracture strain for the model that agrees well with the fracture criterion. Furthermore, when comparing the experimental strain field distribution with the simulated strain field distribution they are very similar, as can be seen in figure 32, which means that the model captures the experimental behavior. This confirms the inhomogeneous nature of the experiment. A similar issue arises with the shear test as the fracture initiation and propagation does not occur in a shear stress state as can be seen in figure 33 and is further illustrated in figure 36. This brings into question whether the shear stress test can actually be considered to be in a shear stress state or if the experiment should be conducted differently. Due to this, approximations of the fracture strain in the plane strain stress state and the instability strain in the shear stress state were made. However, despite the modifications to the fracture surface the results show good agreement with the experimental

data which further emphasizes the inaccuracy of the experimental stress states.

Despite the anisotropy of the material, the GISSMO damage model is isotropic. This will affect the result and reduce the accuracy of the damage model. To remedy this, an extended version of GISSMO can be used where the damage accumulation is orientation dependent.

5.4 Future work

The material model should be further developed by additional testing in directions other than the rolling direction. This would improve accuracy of the anisotropy assessment which could have a remarkable impact on the damage model.

The damage model developed in this work can be further improved by experimental testing and validation. In the pure shear and compressive stress states, the accuracy of the model cannot be determined due to the lack of experimental data available for comparison. Conducting a punching and a compressive experiment would therefore be valuable in order to improve and validate the damage model in shear and compression.

To further improve the model, a full field, three dimensional parameter identification should be conducted in order to include the Lode angle dependency in the optimization algorithm in LS-OPT. This could reduce the issues with the models being in a similar stress state.

Since the damage model is limited to 316 stainless steel, a similar work must be conducted for other materials of interest, such as titanium. In future work, the design of the experiments should be reconsidered and carefully chosen based on the intended use of the damage model. The issues with the plane strain test could be avoided with a differently designed experiment. For example, by changing the radius of the notched section the stress state could approach plane strain. Furthermore, issues with friction modelling in the biaxial bulge test suggest that it may be relevant to further investigate its impact. The biaxial bulge test can also be replaced with a biaxial tensile test and the current shear test can be redesigned.

The mesh regularization requires continued work for element lengths different from the ones investigated in this work. For example, an element length larger than the one used for calibration of the damage model has not been investigated, which would diversify the damage model.

6 Conclusions

The present approach for investigating a strategy for numerical simulations of punching during concurrent pressing of stainless steel sheet metal appears promising for use with other materials. Despite the lack of incorporation of physical mechanisms, the phenomenological GISSMO damage model shows good experimental agreement. The material model can be more carefully calibrated by additional testing in different directions in the sheet metal in order to more accurately assess the material anisotropy. Inherent modelling issues, such as contact and friction conditions as well as difficulties characterizing stress states suggest that experiments should be designed differently.

Before the damage model resulting from this work can be used in the design process it should be validated with physical testing. Despite the results showing a fairly good agreement with the experiments that have been conducted, there is uncertainty about whether the fracture strains have been obtained in the correct stress states. It should be taken into account that there is a lack of comparative data in the shear, compressive and plane strain stress states.

Despite the mentioned issues, this thesis work and the resulting damage model may provide valuable insight into the sheet metal punching process.

References

[1] Markus Avermann. *Why do we still need Forming Limit Diagrams (FLDs)?* 2020. URL: https://formingworld.com/forming-limit-diagram/ (**urlseen** 10/01/2023).

[2] Alfa Laval. *History of Alfa Laval*. 2016. URL: https://www.alfalaval.com/about-us/our-company/history-of-alfa-laval/ (**urlseen** 14/09/2022).

[3] Alfa Laval. *Gasketed plate-and-frame heat exchangers*. URL: https://www.alfalaval.com/products/heat-transfer/plate-heat-exchangers/gasketed-plate-and-frame-heat-exchangers/ (**urlseen** 04/12/2022).

[4] J. Keith Nisbett Richard G. Budynas. *Shigley's Mechanical Engineering Design, 9th Edition*. McGraw Hill, 2011. ISBN: 978–0–07–352928–8.

[5] Niels Saabye Ottosen **and** Matti Ristinmaa. *The Mechanics of Constitutive Modelling*. Elsevier Science, 2005. ISBN: 978-0-08-044606-6.

[6] Wikimedia Commons. *File:Stress transformation 3D.svg*. [Online; accessed 22-December-2022]. 2022. URL: https://commons.wikimedia.org/w/index.php?title=File:Stress_transformation_3D.svg&oldid=665883480.

[7] André Haufe **andothers**. "GISSMO – Material Modeling with a sophisticated Failure Criteria". **in**(**october** 2011): DOI: 10.13140/RG.2.2.27677.92646.

[8] A. C. Mackenzie J. W. Hancock. "On the mechanisms of ductile failure in high strength steels subjected to multi-axial stress states." **in***Journal of the Mechanics and Physics of Solids*: 24 (1976), **pages** 147–160. DOI: https://doi.org/10.1016/0022-5096(76)90024-7.

[9] T. Wierzbicki Y. Bai. "A comparative study of three groups of ductile fracture loci in the 3D space." **in***Engineering Fracture Mechanics*: 135 (2015), **pages** 147–167. DOI: https://doi.org/10.1016/j.engfracmech.2014.12.023.

[10] Liang Xue. "Ductile fracture modeling: Theory, experimental investigation and numerical verification". **in***Massachusetts Institute of Technology*: (**january** 2009).

[11] T. Wierzbicki Y. Bai. "A new model of metal plasticity and fracture with pressure and Lode dependence." **in***International Journal of Plasticity*: 24 (2008), **pages** 1071–1096. DOI: https://doi.org/10.1016/j.ijplas.2007.09.004.

[12] H. H. Wisselink. "Analysis of Guillotining and Slitting". **in**(2008): DOI: ISBN:90365.13995.

[13] P. Ponte Castañeda K. Danas. "Influence of the Lode parameter and the stress triaxiality on the failure of elasto-plastic porous materials". **in***International Journal of Solids and Structures*: 49 (2012), **pages** 1325–1342. DOI: https://doi.org/10.1016/j.ijsolstr.2012.02.006.

[14] D. M. Tracey J. R. Rice. "On the ductile enlargement of voids in triaxial stress fields". **in***Journal of the Mechanics and Physics of Solids*: 17 (1969), **pages** 201–219. DOI: https://doi.org/10.1016/0022-5096(69)90033-7.

[15] N. Saba, M. Jawaid **and** M.T.H. Sultan. "Mechanical and Physical Testing of Biocomposites, Fibre-Reinforced Composites and Hybrid Composites". **inbyeditor**Mohammad Jawaid, Mohamed Thariq **and** Naheed Saba: Woodhead Publishing, 2019, **pages** 1–12. ISBN: 978-0-08-102292-4. DOI: https://doi.org/10.1016/B978-0-08-102292-4.00001-1. URL: https://www.sciencedirect.com/science/article/pii/B9780081022924000011.

[16] L. Pérez Caro **andothers**. "Damage and fracture during sheet-metal forming of alloy 718". **in***International Journal of Material Forming*: (2020). DOI: https://doi.org/10.1007/s12289-018-01461-4.

[17] Ted Sjöberg **andothers**. "Experimental characterisation of the evolution of triaxiality stress state for sheet metal materials". **in***European Journal of Mechanics - A/Solids*: 66 (2017), **pages** 279–286. ISSN: 0997-7538. DOI: https://doi.org/10.1016/j.euromechsol.2017.07.013. URL: https://www.sciencedirect.com/science/article/pii/S099775381730181X.

[18] World Steel Association AISBL. *R-Value*. 2020. URL: https://ahssinsights.org/forming/mechanical-properties/r-value/ (**urlseen** 05/12/2022).

[19] *Least Square Method*. URL: https://www.cuemath.com/data/least-squares/ (**urlseen** 08/12/2022).

[20] R. Panowicz. "Analysis of selected contact algorithms types in terms of their parameters selection". **in***Journal of KONES*: 20 (2013), **pages** 51–66. DOI: 10.5604/12314005.1136172.

[21] Dynamore GmbH. *Contact modeling in LS-DYNA*. URL: https://www.dynasupport.com/tutorial/ls-dyna-users-guide/contact-modeling-in-ls-dyna (**urlseen** 05/12/2022).

[22] H. Olsson **andothers**. "Friction Models and Friction Compensation". **in***European Journal of Control*: 4.3 (1998), **pages** 176–195. DOI: https://doi.org/10.1016/S0947-3580(98)70113-X. URL: https://www.sciencedirect.com/science/article/pii/S094735809870113X.

[23] Long Li **andothers**. "Effects of mass scaling on finite element simulation of the cold roll-beating forming process". **in***IOP Conference Series: Materials Science and Engineering*: 490.5 (**april** 2019), **page** 052019. DOI: 10.1088/1757-899X/490/5/052019. URL: https://dx.doi.org/10.1088/1757-899X/490/5/052019.

[24] Wikimedia Commons. *File:Tresca stress 2D.png*. [Online; accessed 21-December-2022]. 2020. URL: https://commons.wikimedia.org/w/index.php?title=File:Tresca_stress_2D.png&oldid=484477336.

[25] F. Barlat **andothers**. "Plane stress yield function for aluminum alloy sheets—part 1: theory". **in***International Journal of Plasticity*: 19.9 (2003), **pages** 1297–1319. ISSN: 0749-6419. DOI: https://doi.org/10.1016/S0749-6419(02)00019-0. URL: https://www.sciencedirect.com/science/article/pii/S0749641902000190.

[26] Jeong-Whan Yoon **andothers**. "Plane stress yield function for aluminum alloy sheets—part II: FE formulation and its implementation". **in***International Journal of Plasticity*: 20.3 (2004). Owen Richmond Memorial Special Issue, **pages** 495–522. ISSN: 0749-6419. DOI: https://doi.org/10.1016/S0749-6419(03)00099-8. URL: https://www.sciencedirect.com/science/article/pii/S0749641903000998.

[27] S. DiCecco et al. "Numerical and experimental investigation of the formability of AA6013-T6". **in***Journal of Physics: Conference Series*: 896 (2017), **page** 012114. DOI: 10.1088/1742-6596/896/1/012114.

[28] Mikael Schill. *Ductile material failure in LS-DYNA*. Dynamore Nordic AB. 2 **february** 2016. URL: https://files.dynamore.se/index.php/s/j3ofFy7baEkREm3?dir=undefined&path=%5C%2F2_Webinars%5C%2F3_Material_and_Failure%5C%2FDuctile_Failure&openfile=205228 (**urlseen** 14/12/2022).

[29] A. L. Gurson. "Plastic flow and fracture behavior of ductile materials incorporating void nucleation, growth, and interaction." phdthesis. Brown University, 1975.

[30] David Taylor. "CHAPTER 4 - Other Theories of Fracture: A Review of Approaches to Fracture Prediction". **in***The Theory of Critical Distances*: Oxford: Elsevier Science Ltd, 2007, **pages** 51–61. ISBN: 978-0-08-044478-9. DOI: https://doi.org/10.1016/B978-008044478-9/50005-3. URL: https://www.sciencedirect.com/science/article/pii/B9780080444789500053.

[31] A. Haufe F. Neukamm M. Feucht. "Consistent Damage Modelling in the Process Chain of Forming to Crashworthiness Simulations". **in**(2008).

[32] Brandt Humphrey **andothers**. "Improved Methodologies in Modeling and Predicting Failure in AASHTO M-180 Guardrail Steel Using Finite Element Analysis – Phase I." **in**(**august** 2016).

[33] Tomasz Wierzbicki **and** Liang Xue. "On the effect of the third invariant of the stress deviator on ductile fracture". **in***Impact and Crashworthiness Laboratory, Technical Report*: 136 (2005).

[34] J. Lemaitre. "A Continuous Damage Mechanics Model for Ductile Fracture". **in***Journal of Engineering Materials and Technology*: 107 (1985), **pages** 83–89. DOI: https://doi.org/10.1115/1.3225775.

[35] André Haufe **andothers**. “A generalized Stress State dependent Damage Model for Forming and Crashworthiness Simulations”. **in**(**september** 2008).

[36] n.d. *LS-DYNA Keyword User’s Manual, Volume 2, Material Models*. English. **version** LS-DYNA R13. Livermore Software Technology (LST), an Ansys Company. 1993 **pagetotals**. forthcoming.

[37] Bonjoon Gu, Jongmin Lim **and** Seokmoo Hong. “Determination and Verification of GISSMO Fracture Properties of Bolts Used in Radioactive Waste Transport Containers”. **in***Materials*: 15.5 (2022). ISSN: 1996-1944. DOI: 10.3390/ma15051893. URL: https://www.mdpi.com/1996-1944/15/5/1893.

[38] Yuanli Bai **and** Tomasz Wierzbicki. “Application of extended Mohr-Coulomb criterion to ductile fracture”. **in***International Journal of Fracture*: 161 (**november** 2010), **pages** 1–20. DOI: 10.1007/s10704-009-9422-8.